# 1

# Basic Principles



## 1.1 Introduction

The field of spectroscopy is in general concerned with the interaction between matter and electromagnetic radiation. Atoms and molecules have a range of discrete energy levels corresponding to different electronic, vibrational or rotational states. The interaction between atoms and electromagnetic radiation is characterized by the absorption and emission of photons, such that the energy of the photons exactly matches an energy level difference in the atom. Since the energy of a photon is proportional to the frequency, the different forms of spectroscopy are often distinguished on the basis of the frequencies involved. For instance, absorption and emission between electronic states of the outer electrons typically require frequencies in the ultraviolet (UV) range, hence giving rise to UV spectroscopy. Molecular vibrational modes are characterized by frequencies just below visible red light and are thus studied with infrared (IR) spectroscopy. Nuclear magnetic resonance (NMR) spectroscopy uses radiofrequencies, which are typically in the range of 10–800 MHz.

NMR is the study of the magnetic properties (and energies) of nuclei. The absorption and emission of electromagnetic radiation can be observed when the nuclei are placed in a (strong) external magnetic field. Purcell, Torrey and Pound [1] at MIT, Cambridge and Bloch, Hansen and Packard [2] at Stanford simultaneously, but independently discovered NMR in 1946. In 1952 Bloch and Purcell shared the Nobel Prize for physics in recognition of their pioneering achievements [1–4]. At this stage, NMR was purely an experiment for physicists to determine the nuclear magnetic moments of nuclei. NMR could only develop into one of the most versatile forms of spectroscopy after the discovery that nuclei within the same molecule absorb energy at different resonance frequencies. These so-called chemical shift effects, which are directly related to the chemical environment of the nuclei, were first observed in 1950 by Proctor and Yu [5], and independently by Dickinson [6].

In the first two decades, NMR spectra were recorded in a continuous wave mode in which the magnetic field strength or the radiofrequency (RF) was swept through the spectral area

In Vivo *NMR Spectroscopy – 2nd Edition: Principles and Techniques* Robin A. de Graaf

of interest, whilst keeping the other fixed. In 1966, NMR was revolutionized by Ernst and Anderson [7] who introduced pulsed NMR in combination with Fourier transformation. Pulsed or Fourier transform NMR is at the heart of all modern NMR experiments.

The induced energy level difference of nuclei in an external magnetic field is very small when compared with the thermal energy, making it that the energy levels are almost equally populated. As a result the absorption of photons is very low, making NMR a very insensitive technique when compared with the other forms of spectroscopy. However, the low energy absorption makes NMR also a noninvasive and nondestructive technique, ideally suited for *in vivo* measurements. It is believed that, by observing the water signal from his own finger, Bloch was the first to use NMR on a living system. Soon after the discovery of NMR, others showed the utility of using NMR to study living objects. In 1950, Shaw and Elsken [8] used proton NMR to investigate the water content of vegetable material. Odebald and Lindstrom [9] obtained proton NMR signals from a number of mammalian preparations in 1955. Continued interest in defining and explaining the properties of water in biological tissues led to the promising report of Damadian in 1971 [10] that NMR properties (relaxation times) of malignant tumorous tissue significantly differs from normal tissue, suggesting that (proton) NMR may have diagnostic value. In the early 1970s, the first experiments of NMR spectroscopy on intact living tissues were reported. Moon and Richards [11] used $^{31}$P NMR on intact red blood cells and showed how the intracellular pH can be determined from chemical shift differences. In 1974, Hoult *et al*. [12] reported the first study of $^{31}$P NMR to study intact, excised rat hind leg.

Around the same time reports on *in vivo* NMR spectroscopy appeared, Lauterbur [13] and Mansfield and Grannell [14] described the first reports of a major application of modern NMR, namely *in vivo* NMR imaging or magnetic resonance imaging (MRI). By applying position dependent magnetic fields in addition to the static magnetic field, they were able to reconstruct the spatial distribution of the spins in the form of an image. Lauterbur and Mansfield shared the 2003 Nobel Prize in medicine. *In vivo* NMR spectroscopy or magnetic resonance spectroscopy (MRS) and MRI have evolved from relatively simple one or two RF pulse sequences to complex techniques involving spatial localization, water and lipid suppression and spectral editing for MRS and time-varying magnetic field gradients, ultra fast and multiparametric acquisition schemes for MRI.

In this chapter the basic phenomenon of NMR is considered. After establishing the Larmor resonance condition with a combination of classical and quantum mechanical arguments, the NMR phenomenon is approached from a more practical point of view with the aid of the macroscopic Bloch equations. The phenomena of chemical shift, scalar coupling and spin echoes will be described, as well as some elementary processing of the NMR signal.

## 1.2 Classical Description

NMR is based on the concept of nuclear spin. Before discussing the properties of nuclear spins, some relations from classical physics will be introduced which will simplify further discussions. Although classical physics is incapable of describing the quantum mechanical spin, it can be used to create a familiar frame of reference in which the existence of a spin angular momentum can be visualized.

Motion (linear or rotational) always has a corresponding momentum (linear or angular). For an object of mass m and velocity **v**, the linear momentum **p** is given by:

$$\mathbf{p} = \mathrm{m}\mathbf{v} \tag{1.1}$$

Conceptually, momentum can be thought of as the tendency for an object to continue its motion. The momentum only changes when an external force **F** is applied, in accordance with Newton's second law:

$$\mathbf{F} = \left(\frac{\mathrm{d}\mathbf{p}}{\mathrm{dt}}\right) = \mathrm{m}\mathbf{a} \tag{1.2}$$

where **a** is the acceleration. In the absence of external forces, the object does not accelerate (or decelerate) and the linear momentum and hence the speed is constant.

Now consider an object rotating with constant velocity about a fixed point at a distance **r**. This motion is described with an angular momentum vector **L**, defined as:

$$\mathbf{L} = \mathbf{r} \times \mathbf{p} \tag{1.3}$$

Therefore, the magnitude of **L** is mvr and its direction is perpendicular to the plane of motion. Angular momentum can only be changed when an external torque is applied, in analogy with the application of force on a linear momentum. Torque **T** (or rotational force) is defined as the cross product of force and the distance over which the force has to be delivered:

$$\mathbf{T} = \mathbf{r} \times \mathbf{F} = \mathbf{r} \times \left(\frac{\mathrm{d}\mathbf{p}}{\mathrm{dt}}\right) = \left(\frac{\mathrm{d}\mathbf{L}}{\mathrm{dt}}\right) \tag{1.4}$$

Now suppose that the rotating object carries an electrical charge so that a current loop is created. According to classical physics this current generates a magnetic field, which is characterized by the magnetic dipole moment, $\boldsymbol{\mu}$, a fundamental magnetic quantity associated with the current. In general the magnetic moment $\boldsymbol{\mu}$ is given by:

$$\boldsymbol{\mu} = [\text{current}][\text{area}] \tag{1.5}$$

For an object of mass m and charge e rotating at constant rotational velocity **v** about a fixed point at distance **r**, the magnetic moment $\boldsymbol{\mu}$ is given by:

$$\boldsymbol{\mu} = \left[\frac{\mathrm{e}\mathbf{v}}{2\pi\mathbf{r}}\right]\pi\mathbf{r}^2 \tag{1.6}$$

Using $\mathbf{L} = \mathrm{m}\mathbf{v}\mathbf{r}$, a fundamental relation between magnetic moment and angular moment is obtained:

$$\boldsymbol{\mu} = \left(\frac{\mathrm{e}}{2\mathrm{m}}\right)\mathbf{L} = \gamma\mathbf{L} \tag{1.7}$$

where $\gamma$ is the (classical) gyromagnetic ratio. It turns out that relation (1.7) is valid for any periodic, orbital motion, including microscopic motion of elementary particles. In the next section it is shown that relation (1.7) is also obtained when using quantum mechanical arguments. When the rotating object is placed in an external magnetic field $\mathbf{B}_0$, the loop will feel a torque given by:

$$\mathbf{T} = \boldsymbol{\mu} \times \mathbf{B}_0 \tag{1.8}$$

Combining Equations (1.4), (1.7) and (1.8) gives:

$$\left(\frac{d\boldsymbol{\mu}}{dt}\right) = \gamma\,\boldsymbol{\mu} \times \mathbf{B}_0 \tag{1.9}$$

Since the amplitude of $\boldsymbol{\mu}$ is constant, the differential equation in Equation (1.9) expresses the fact that $\boldsymbol{\mu}$ changes its orientation relative to $\mathbf{B}_0$, i.e. $\boldsymbol{\mu}$ rotates (precesses) about $\mathbf{B}_0$. Alternatively, a precession of $\boldsymbol{\mu}$ about $\mathbf{B}_0$ can be described by:

$$\left(\frac{d\boldsymbol{\mu}}{dt}\right) = \boldsymbol{\mu} \times \boldsymbol{\omega}_0 \tag{1.10}$$

Combining Equations (1.9) and (1.10) results in the famous Larmor equation:

$$\boldsymbol{\omega}_0 = \gamma \mathbf{B}_0$$

or

$$\boldsymbol{\nu}_0 = \left(\frac{\boldsymbol{\omega}_0}{2\pi}\right) = \left(\frac{\gamma}{2\pi}\right)\mathbf{B}_0 \tag{1.11}$$

The precession (or Larmor) frequency $\nu_0$ is thus directly proportional to the applied magnetic field $\mathbf{B}_0$ and also to the gyromagnetic ratio $\gamma$ (or $\boldsymbol{\mu}$), which is characteristic for the nucleus under investigation.

A magnetic moment in an external magnetic field also has an associated magnetic energy defined as:

$$E = -\boldsymbol{\mu} \cdot \mathbf{B}_0 = -\mu B_0 \cos\theta \tag{1.12}$$

where $\theta$ is the angle between the magnetic moment $\boldsymbol{\mu}$ and the external magnetic field $\mathbf{B}_0$. Equation (1.12) indicates that the magnetic energy is minimized when $\boldsymbol{\mu}$ is parallel with $\mathbf{B}_0$ ($\theta = 0^\circ$) and maximized when $\boldsymbol{\mu}$ is antiparallel with $\mathbf{B}_0$ ($\theta = 180^\circ$). According to Equation (1.12), the classical magnetic moment may assume any orientation ($0^\circ \leq \theta \leq 180^\circ$), with energy varying between $+\mu B_0$ and $-\mu B_0$. Therefore, even though classical mechanics can create a familiar picture of the relation between angular momentum, magnetic moment and Larmor frequency, it cannot explain how the general resonance condition for spectroscopy, $\Delta E = h\nu$, relates to the magnetic energy associated with the magnetic moment. A quantum mechanical treatment is necessary to obtain information about the interaction of electromagnetic waves and nuclear spins. In the next section basic quantum mechanical concepts are introduced, after which the NMR resonance condition is derived.

## 1.3 Quantum Mechanical Description

One of the fundamental postulates in quantum mechanics is that the angular momentum of elementary particles (be it protons, neutrons, or electrons) is limited to discrete values, i.e. the angular momentum $\mathbf{L}$ is quantized and its amplitude is given by:

$$L = \left(\frac{h}{2\pi}\right)\sqrt{I(I+1)} \tag{1.13}$$

where I is the spin quantum number, which can only be integral or half-integral and h is Planck's constant. Since angular momentum is a vector, the full description of $\mathbf{L}$ must

involve its amplitude, given by Equation (1.13), and its direction. In quantum mechanics the direction of angular momentum is specified by a second quantum number m, which can only have certain discrete orientations with respect to a given direction. The component of angular momentum in the z direction, $L_z$, is given by:

$$L_z = \left(\frac{h}{2\pi}\right) m \tag{1.14}$$

Quantum mechanics shows that m can have 2I+1 values, given by:

$$m = I,\ I-1,\ I-2, \ldots, -I \tag{1.15}$$

For protons, neutrons and electrons, the spin quantum number I equals 1/2. For nuclei, I cannot simply be calculated by summation of its individual components. However, by using the atomic mass and the charge number, I can be deduced from the following rules:

1. For nuclei with an odd mass number, I is half-integral (1/2, 3/2, 5/2, . . . , e.g. $^{1}H$, $^{13}C$, $^{15}N$, $^{23}Na$, $^{31}P$).
2. For nuclei with an even mass number and an even charge number, I is zero (e.g. $^{12}C$, $^{16}O$, $^{32}S$).
3. For nuclei with an even mass and an odd charge number I is an integral number (1, 2, . . . , e.g. $^{2}H$, $^{14}N$).

By analogy with Equation (1.7), elementary particles also have a magnetic moment $\boldsymbol{\mu}$ which is related to the angular momentum $\mathbf{L}$ through:

$$\boldsymbol{\mu} = \gamma \mathbf{L} \tag{1.16}$$

where $\gamma$ is again the gyromagnetic ratio. Since the angular momentum is quantized, the magnetic moment will also be quantized. The component of the magnetic moment along the longitudinal z axis is given [by analogy with Equation (1.14)] by:

$$\mu_z = \gamma \left(\frac{h}{2\pi}\right) m \tag{1.17}$$

where m is given by Equation (1.15). In an external magnetic field $\mathbf{B}_0$, the particle acquires a magnetic energy given by Equation (1.12). Combining this classical description of the magnetic energy with the quantum mechanical formulation of magnetic moment gives:

$$E = -\mu_z B_0 = -\gamma \left(\frac{h}{2\pi}\right) m B_0 \tag{1.18}$$

Since m is a discrete quantum number [see Equation (1.15)], the energy levels are also quantized. For a particle of spin I = 1/2, there are only two energy levels (m = –1/2 and +1/2) and the energy difference $\Delta E$ is given by (see Figure 1.1):

$$\Delta E = \gamma \left(\frac{h}{2\pi}\right) B_0 \tag{1.19}$$

The resonance phenomenon in NMR is achieved by applying an oscillating magnetic field perpendicular to $\mu_z$ with a frequency $\nu_0$, such that the energy equals the magnetic energy

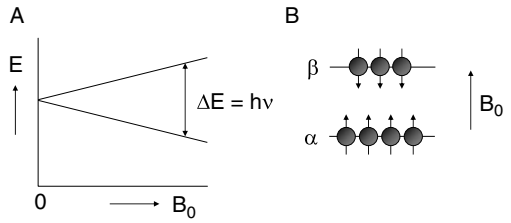


***Figure 1.1*** *(A) The nuclear spin energy for a spin-1/2 nucleus as a function of the external magnetic field strength $B_0$. (B) The lower energy level ($\alpha$ spin state) corresponds to magnetic moments parallel with $B_0$, while spins in the higher energy level ($\beta$ spin state) have an antiparallel alignment with $B_0$. For all currently available magnets, the energy level difference between the two spin states corresponds to electromagnetic radiation in the RF range.*

given by Equation (1.19), i.e. the energy of the electromagnetic wave is given by:

$$\Delta E = h\nu_0 \tag{1.20}$$

Combining Equations (1.19) and (1.20) will give the earlier derived Larmor equation:

$$\nu_0 = \left(\frac{\gamma}{2\pi}\right) B_0 \tag{1.21}$$

Even though the classical and quantum mechanical descriptions of NMR lead to the same result, they play a different role in the understanding of the technique. Quantum mechanics is the only theory which can quantitatively describe the NMR phenomenon. Classical principles are mainly used to visualize the effects of RF pulses on macroscopic magnetization vectors.

## 1.4 Macroscopic Magnetization

Figure 1.2A shows the precession (at the Larmor frequency) of a magnetic moment around an external magnetic field according to classical principles. Quantization of magnetic moment (and magnetic energy) can readily be incorporated in this picture. For elementary particles the angle $\theta$ between $\boldsymbol{\mu}$ and $\mathbf{B}_0$ can no longer be arbitrary as in Section 1.2 but is given by:

$$\cos\theta = \frac{m}{\sqrt{I(I+1)}} \tag{1.22}$$

For a nucleus of spin $I = 1/2$, $m = +1/2$ or $-1/2$ yielding an angle $\theta = 54.74^\circ$ relative to the $+z$ or $-z$ axis, respectively. Therefore, the nuclei of spin $I = 1/2$ are distributed on the surface of two cones, and rotate about $\mathbf{B}_0$ at the Larmor frequency (Figure 1.2B). In the general case of a spin I nucleus, the magnetic moments will be distributed on $2I+1$ cones at discrete angles $\theta$ as defined by Equation (1.22). For a spin 1/2 nucleus the two spin states $m = +1/2$ ($\boldsymbol{\mu}$ parallel with $\mathbf{B}_0$) and $m = -1/2$ ($\boldsymbol{\mu}$ antiparallel to $\mathbf{B}_0$) are often referred to as the $\alpha$ and $\beta$ spin states, respectively.

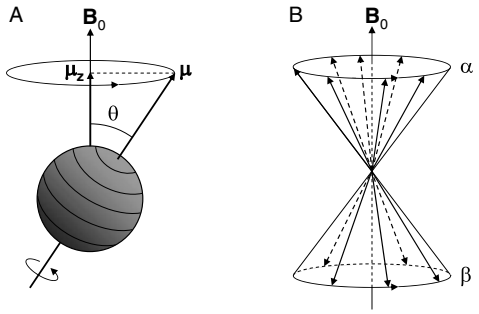


***Figure 1.2*** *(A) A nuclear spin precessing in an external magnetic field* $\mathbf{B}_0$*. The spin magnetic moment* $\boldsymbol{\mu}$ *precesses about* $\mathbf{B}_0$*, in which the orientation* $\theta$ *and the amplitude (along z)* $\mu_z$ *are quantized. (B) In a macroscopic ensemble of nuclear spin-1/2, the spins distribute themselves among two possible orientations according to the Boltzmann equation.*

So far, only the behavior of individual nuclear spins has been considered. However, a macroscopic sample contains many spins, which will be randomly distributed on the cones. As a consequence of the small energy difference between the spin states there will be a small difference in the population of these spin states. This population difference can be calculated using the Boltzmann equation. For the situation shown in Figure 1.2B the energy difference $\Delta E = h\nu$ gives rise to a population distribution given by:

$$\left(\frac{n_\alpha}{n_\beta}\right) = e^{\Delta E/kT} = e^{h\nu/kT} \tag{1.23}$$

where $n_\alpha$ is the number of spins in the $\alpha$ (low energy) state, $n_\beta$ is the number of spins in the $\beta$ (high energy state), k is the Boltzmann constant and T is the absolute temperature. Since at normal temperature, $h\nu$ is much less than the thermal energy kT, the exponent in Equation (1.23) can be simplified through an expansion and truncation of a Taylor series to give:

$$\left(\frac{n_\alpha}{n_\beta}\right) = 1 + \left(\frac{h\nu}{kT}\right) \tag{1.24}$$

For a macroscopic sample containing one million nuclear spins at 37 °C (T = 310.15 K) and in a magnetic field of 9.4 T, corresponding to $\nu = 400$ MHz, the population difference between the $\alpha$ and $\beta$ spin states is only 31 spins (corresponding to 0.0031 %). Since the final received signal is proportional to the population difference, NMR is a rather insensitive technique compared with other forms of spectroscopy, where the energy difference is much larger.

The total net magnetic moment (i.e. 'the magnetization'), **M**, of a macroscopic sample is the resultant of the sum over all individual magnetic moments $\boldsymbol{\mu}$. Since the magnetic moments are randomly distributed on the cones, there will be no net component of **M** in the transverse xy plane (see Figure 1.2B). However, due to the population difference there will be a net component of **M** parallel with $\mathbf{B}_0$ along the +z axis. At thermal equilibrium

the magnitude of the longitudinal magnetization, $\mathbf{M}_0$ is:

$$M_0 = \sum_{i=1}^{n} \mu_i = n_\alpha \mu_z + n_\beta \mu_z = \gamma \left(\frac{h}{4\pi}\right)(n_\alpha - n_\beta) \tag{1.25}$$

Using Equation (1.24), $(h\nu/kT) \ll 1$ and $n = n_\alpha + n_\beta$ where n is the total number of nuclear spins in the macroscopic sample, the population difference $(n_\alpha - n_\beta)$ is given by:

$$(n_\alpha - n_\beta) \approx \left(\frac{nh\nu}{2kT}\right) \tag{1.26}$$

Therefore, at thermal equilibrium, the amplitude of the macroscopic magnetization vector $\mathbf{M}_0$ is:

$$M_0 = \left(\frac{\gamma h}{2\pi}\right)^2 \left(\frac{nB_0}{4kT}\right) \tag{1.27}$$

From Equation (1.27) several important features concerning the sensitivity of NMR experiments can be deduced. The quadratic dependence of $\mathbf{M}_0$ on the gyromagnetic ratio $\gamma$ implies that nuclei resonating at high frequency [see Equation (1.11)] also generate relatively intense NMR signals. Hydrogen has the highest $\gamma$ of the commonly encountered nuclei, and has therefore the highest relative intensity. The linear dependence of $\mathbf{M}_0$ on the magnetic field strength $\mathbf{B}_0$ implies that higher magnetic fields improve the sensitivity. In fact this argument (and the related increase in chemical shift dispersion) has caused a steady drive towards higher magnetic field strength which now typically range from 1.5 T to 17.5 T (or up to circa 11.7 T for *in vivo* applications). Finally, the inverse proportionality of $\mathbf{M}_0$ to the temperature T indicates that sensitivity can be enhanced at lower sample temperatures. Obviously, the latter option is unrealistic for *in vivo* applications.

The actual experimental sensitivity is determined by many factors, like sample volume, gyromagnetic ratio, natural abundance of the nucleus studied, (sample) noise, relaxation parameters and magnetic field strength. Although some factors can be predicted by Equation (1.27), others (e.g. noise) need a more detailed treatment which will be given in Chapter 10. The intrinsic sensitivities of the most relevant nuclei encountered in *in vivo* NMR spectroscopy are summarized in Table 1.1.

## 1.5 Excitation

In NMR experiments, macroscopic samples are studied, containing many individual spins. Figure 1.2B demonstrates clearly how the spin angular moments are distributed on a discrete number of cones. The quantum mechanical representation is convenient to illustrate the spin distribution, but it is not very suitable to illustrate the interaction of the spins with external magnetic fields. Therefore the classical picture of the net macroscopic magnetization vector $\mathbf{M}_0$ will be used in further discussions.

In order to observe nuclear magnetization, the precessional motion needs to be detected. However, at thermal equilibrium the spins have no phase coherence in the transverse plane and the net longitudinal magnetization is a static vector. Nuclear magnetization can only be observed by rotating the net longitudinal magnetization towards or onto the transverse plane. This can be accomplished by a second magnetic field in the transverse plane

***Table 1.1*** *NMR properties of commonly encountered nuclei in in vivo NMR*

| Isotope | Spin | Gyromagnetic ratio ($10^7$ rad $T^{-1}$ $s^{-1}$) | NMR frequency at 2.35 T (MHz) | Natural abundance (%) | Relative sensitivity[a] |
|---|---|---|---|---|---|
| $^{1}H$ | 1/2 | 26.752 | 100.000 | 99.985 | 1.00 |
| $^{2}H$ | 1 | 4.107 | 15.351 | 0.015 | $1.45 \times 10^{-6}$ |
| $^{3}He$ | 1/2 | −20.380 | 76.181 | $1.4 \times 10^{-4}$ | $5.75 \times 10^{-7}$ |
| $^{7}Li$ | 3/2 | 10.398 | 38.866 | 92.58 | 0.272 |
| $^{13}C$ | 1/2 | 6.728 | 25.145 | 1.108 | $1.76 \times 10^{-4}$ |
| $^{14}N$ | 1 | 1.934 | 7.228 | 99.630 | $1.00 \times 10^{-3}$ |
| $^{15}N$ | 1/2 | −2.712 | 10.137 | 0.370 | $3.86 \times 10^{-6}$ |
| $^{17}O$ | 5/2 | −3.628 | 13.562 | 0.037 | $1.08 \times 10^{-5}$ |
| $^{19}F$ | 1/2 | 25.181 | 94.094 | 100.000 | 0.834 |
| $^{23}Na$ | 3/2 | 7.080 | 26.466 | 100.000 | $9.27 \times 10^{-2}$ |
| $^{31}P$ | 1/2 | 10.841 | 40.481 | 100.000 | $6.65 \times 10^{-2}$ |
| $^{39}K$ | 3/2 | 1.250 | 4.672 | 93.100 | $4.75 \times 10^{-4}$ |
| $^{129}Xe$ | 1/2 | −7.452 | 27.856 | 26.44 | $5.71 \times 10^{-3}$ |

[a] Relative sensitivity is calculated as the product of NMR sensitivity (proportional to $|\gamma^3| \times I(I+1)$) and the natural abundance.

oscillating in the RF (MHz) range, i.e. $B_{1max}\cos(\omega t)$, where $B_{1max}$ is the amplitude of the applied field and $\omega$ its frequency. In modern Fourier transform NMR, the $B_1$ field is applied as a RF pulse (i.e. turned on for a finite time T and turned off again). During the RF pulse, the magnetization will precess about $\mathbf{B}_0$ and $\mathbf{B}_1$. Throughout this chapter and the remainder of the book anticlockwise rotations will be used in accordance with the theory first developed by Bloch [2–4]. The initially longitudinal magnetization experiences a torque from the applied $\mathbf{B}_1$ field, which results in a rotation of $\mathbf{M}_0$ towards the transverse plane (Figure 1.3). Because two external magnetic fields act simultaneously

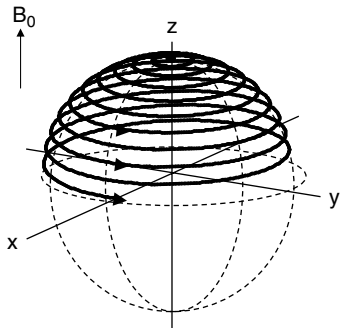


***Figure 1.3*** *Excitation of magnetization in the nonrotating, laboratory frame xyz. The longitudinal magnetization $\mathbf{M}_0$, initially aligned with the z axis, will precess about the static magnetic field $\mathbf{B}_0$ and the irradiating RF field $\mathbf{B}_1$ in the transverse plane. This results in a rotation towards the transverse plane due to $\mathbf{B}_1$ and a simultaneous precession at the Larmor frequency about $\mathbf{B}_0$. In this case $\mathbf{B}_1$ was calibrated to rotate $\mathbf{M}_0$ by 90° away from the z axis to give complete excitation.*

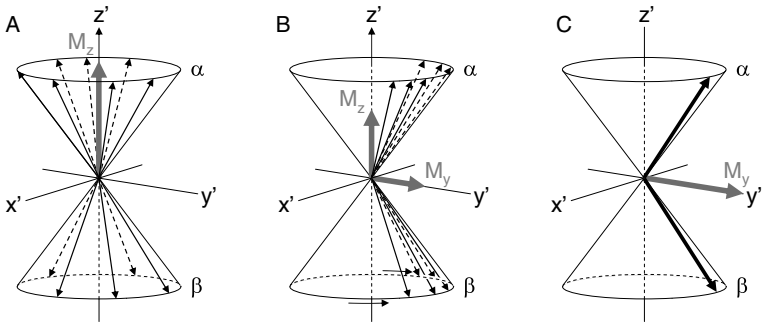


***Figure 1.4*** *Excitation of magnetization in the rotating frequency frame of reference x′y′z′. (A) At thermal equilibrium the Boltzmann distribution of individual nuclear spins in a macroscopic sample creates a net magnetization vector along +z′. Since the individual spins have no phase coherence (i.e. their phases are randomly distributed), there is no net magnetization in the transverse plane. (B) A magnetic field* $\boldsymbol{B}_1$ *along −x′ rotates the net macroscopic magnetization towards +y′. On the microscopic level this is equivalent to the generation of phase coherence between the individual spins. (C) When the magnetic field* $\boldsymbol{B}_1$ *is calibrated to give complete excitation, the spins have attained complete phase coherence resulting in a net magnetization vector along +y′. No magnetization remains along z′.*

on $\mathbf{M}_0$, the rotation of $\mathbf{M}_0$ during the applied $\mathbf{B}_1$ field appears to be rather complex. In Section 1.6 the concept of rotating frames of reference will be introduced which considerably simplifies the rotations. When the applied $\mathbf{B}_1$ field is applied long enough, $\mathbf{M}_0$ can be completely excited onto the transverse plane or even inverted to the -z axis, giving rise to so-called 90° excitation and 180° inversion RF pulses, respectively. Following the pulse, the magnetization experiences only the main magnetic field $\mathbf{B}_0$ and will precess around it with the Larmor frequency. For the observant reader the rotation of magnetization towards the transverse plane may seem in violation with the quantum mechanical property of spins to be either parallel or antiparallel with the main magnetic field $\mathbf{B}_0$. However, a link between individual spins, which can only be parallel or antiparallel to the static magnetic field, and macroscopic transverse magnetization can still be understood with a classical description. Figure 1.4 shows an ensemble of individual spins at thermal equilibrium, i.e. the phase of the spins is random such that the net transverse magnetization is zero. Application of a perpendicular RF magnetic field has two effects on the spins. First, the two spin states become more equally populated as a 90° nutation (rotation) angle is approached and second the spins come into a state of phase coherence [15], i.e. the external magnetic field forces the phases of the spins to attain coherence thereby generating transverse magnetization. The transverse magnetization coherently rotates about $\mathbf{B}_0$ at the Larmor frequency $\nu_0$ and induces an electromotive force (emf) in the receiver coil surrounding the sample. The amplitude of the induced emf is determined by Faraday's law of elctromagnetic induction. After amplification this induced emf gives directly rise to the NMR signal. Sections 1.7 and 1.9 will deal with the processing of NMR signal to recognizable spectra and Chapter 10 will deal will the theory of detection systems and coils.

## 1.6 Bloch Equations

In Section 1.2 it was shown that, when placed in a magnetic field **B**, a magnetic moment $\boldsymbol{\mu}$ experiences a torque which is proportional to the time derivative of the angular momentum [Equations (1.4) and (1.8)]. Utilizing the fact that the magnetization is the sum over all magnetic moments, i.e. Equation (1.25), the expression of motion for a single magnetic moment can be generalized for the total magnetization, giving:

$$\frac{d\mathbf{M}(t)}{dt} = \mathbf{M}(t) \times \gamma \mathbf{B}(t) \tag{1.28}$$

where $\mathbf{B}(t)$ may include time-varying components in addition to the static magnetic field $\mathbf{B}_0$. At thermal equilibrium, in the absence of additional (time-varying) magnetic fields, Equation (1.28) simply expresses the fact that the z component of the magnetization **M** is constant, i.e.:

$$\frac{dM_z(t)}{dt} = 0 \tag{1.29}$$

No net x and y components of **M** exist at thermal equilibrium, and therefore no NMR signal can be detected. As qualitatively illustrated in Figure 1.3, the longitudinal magnetization $\mathbf{M}_z$ must be rotated onto the transverse plane, after which the rotating transverse magnetization will induce signal in a receive coil through Faraday's law of induction. From Equation (1.28) it follows that $\mathbf{M}_z$ can be perturbed by a second magnetic field perpendicular to $\mathbf{M}_z$ and since this field is rotating at the Larmor frequency in the RF range of the electromagnetic spectrum, it is often referred to as a RF magnetic field.

The magnetic component of a RF field that is linearly polarized along the x axis in the laboratory frame can be written as:

$$\mathbf{B}_1(t) = 2B_{1\,max} \cos \omega t[\mathbf{x}] \tag{1.30}$$

where $B_{1max}$ is the maximum amplitude of the applied field, $\omega$ is the angular transmitter or carrier frequency of the RF field and $[\mathbf{x}]$ represents a unit vector along the x axis. The linearly polarized field can be decomposed into two circularly polarized fields rotating in opposite direction about the z axis (Figure 1.5) according to:

$$\mathbf{B}_1(t) = B_{1\,max}(\cos \omega t[\mathbf{x}] + \sin \omega t[\mathbf{y}]) + B_{1\,max}(\cos \omega t[\mathbf{x}] - \sin \omega t[\mathbf{y}]) \tag{1.31}$$

Only the field rotating in the same sense as the magnetic moment interacts significantly with the magnetic moment. The counter rotating field influences the spins to the order $(B_1/2B_0)^2$, which is typically a very small number known as the Bloch–Siegert shift [16]. Since under most conditions the counter rotating field can be ignored, the linearly polarized RF field of Equation (1.31) is then equivalent to a rotating magnetic field given by:

$$\mathbf{B}_{1x}(t) = B_{1\,max}(\cos\ \omega t[\mathbf{x}] - \sin \omega t[\mathbf{y}]) = B_{1x} \cos \omega t + B_{1y} \sin \omega t \tag{1.32}$$

A similar expression can be derived for $B'_{1y}(t)$.

In the presence of two magnetic fields $\mathbf{B}_0$ and $\mathbf{B}_1$, Equation (1.28) can be expanded to yield the Bloch equations in the laboratory frame of reference in the absence of

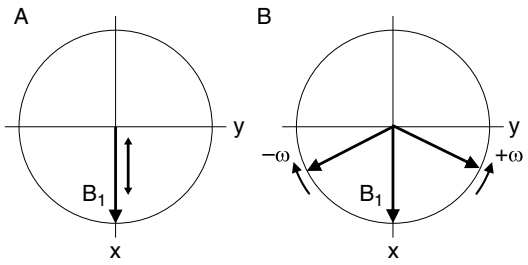


***Figure 1.5*** *Decomposition of a linear oscillating magnetic field (A) into two rotating magnetic fields (B) with frequencies* $-\omega$ *and* $+\omega$*, respectively.*

relaxation [3]:

$$\frac{dM_x(t)}{dt} = \gamma[M_y(t)B_0 - M_z(t)B_{1y}] \tag{1.33}$$

$$\frac{dM_y(t)}{dt} = \gamma[M_z(t)B_{1x} - M_x(t)B_0] \tag{1.34}$$

$$\frac{dM_z(t)}{dt} = \gamma[M_x(t)B_{1y} - M_y(t)B_{1x}] \tag{1.35}$$

Relaxation is the process of return to thermal equilibrium after a perturbation. Components of the magnetization $\mathbf{M}$ (i.e. $\mathbf{M}_x$, $\mathbf{M}_y$ and $\mathbf{M}_z$) return to thermal equilibrium in an exponential manner. The components perpendicular (i.e. $\mathbf{M}_x$ and $\mathbf{M}_y$) and parallel (i.e. $\mathbf{M}_z$) to $\mathbf{B}_0$ relax with different time constants. The relaxation process can be written as:

$$\frac{dM_x(t)}{dt} = -\frac{M_x(t)}{T_2} \tag{1.36}$$

$$\frac{dM_y(t)}{dt} = -\frac{M_y(t)}{T_2} \tag{1.37}$$

$$\frac{dM_z(t)}{dt} = -\frac{M_z(t) - M_0}{T_1} \tag{1.38}$$

$T_1$ and $T_2$ are relaxation time constants. $T_1$ is the longitudinal relaxation time (or spin-lattice relaxation time) and describes the return of longitudinal magnetization after a perturbation. $T_1$ relaxation is in principle a process in which energy from the spins is transferred to the surrounding 'lattice' (which can be either solid or liquid). $T_2$ is the transverse relaxation time (or spin-spin relaxation time) and describes the disappearance of transverse magnetization. $T_2$ relaxation is an entropy-process, since spins exchange energy between themselves (there is no net energy transfer) causing a decrease in phase coherence (i.e. an increase in global chaos or entropy). $T_1$ and $T_2$ relaxation processes in biological tissues are discussed in detail in Chapter 3. Combining Equations (1.33)–(1.35) and Equations (1.36)–(1.38) yields the complete Bloch equations in the laboratory

frame [3]:

$$\frac{dM_x(t)}{dt} = \gamma[M_y(t)B_0 - M_z(t)B_{1y}] - \frac{M_x(t)}{T_2} \tag{1.39}$$

$$\frac{dM_y(t)}{dt} = \gamma[M_z(t)B_{1x} - M_x(t)B_0] - \frac{M_y(t)}{T_2} \tag{1.40}$$

$$\frac{dM_z(t)}{dt} = \gamma[M_x(t)B_{1y} - M_y(t)B_{1x}] - \frac{(M_z(t) - M_0)}{T_1} \tag{1.41}$$

Until this point the NMR experiment has been described in a Cartesian frame fixed with respect to the laboratory (i.e. the 'laboratory' frame). It turns out to be more convenient to describe NMR in a rotating frame. Therefore, consider a new set of Cartesian axes (x′, y′ and z′) rotating about the static magnetic field $\mathbf{B}_0$ with frequency $\omega$. The z and z' axes of the laboratory and rotating frames, respectively, are collinear with the external magnetic field $\mathbf{B}_0$. The components of the magnetization in the rotating frame are given by:

$$M'_x = M_x \cos \omega t + M_y \sin \omega t \tag{1.42}$$

$$M'_y = M_y \cos \omega t - M_x \sin \omega t \tag{1.43}$$

$$M'_z = M_z \tag{1.44}$$

Therefore, using Equations (1.42)–(1.44) the Bloch equations in the rotating frame can be calculated from Equations (1.39)–(1.41), i.e.:

$$\frac{dM'_x(t)}{dt} = -(\omega_0 - \omega)M'_y(t) - \gamma B'_{1y}M'_z(t)\frac{M'_x(t)}{T_2} \tag{1.45}$$

$$\frac{dM'_y(t)}{dt} = (\omega_0 - \omega)M'_x(t) + \gamma B'_{1x}M'_z(t) - \frac{M'_y(t)}{T_2} \tag{1.46}$$

$$\frac{dM'_z(t)}{dt} = \gamma B'_{1y}M'_x(t) - \gamma B'_{1x}M'_y(t) - \frac{(M'_z(t) - M_0)}{T_1} \tag{1.47}$$

where the definitions of $B'_{1x}$ and $B'_{1y}$ as specified in Equation (1.32) are used. In all following text the prime will be omitted as it is assumed that the magnetization vector evolves in the rotating frame of reference. The conversion to a rotating frame of reference has consequences for the magnetic field vectors encountered in that frame. In a frame that rotates with a frequency equal to the frequency of $\mathbf{B}_1$, $\mathbf{B}_1$ appears static. Furthermore, the precessional motion of the magnetization (i.e. $\omega_0 = -\gamma B_0$) appears to be reduced to a value $(\omega_0 - \omega)$. Figure 1.6A shows the generation of transverse magnetization for $\omega = \omega_0$. Since the vectors are drawn in the rotating frame of reference, the magnetization simply precesses about the applied $\mathbf{B}_1$ field towards the transverse plane. Comparison with Figure 1.3, which shows the same situation in the laboratory frame illustrates the clarity of a rotating frame. It is convenient to define an effective magnetic field $\mathbf{B}_e$, which is the vector sum of $(\omega_0 - \omega)/\gamma$ and $\mathbf{B}_1$, since the magnetization precesses about the effective field. The magnitude of $\mathbf{B}_e$ is given by

$$B_e = |\mathbf{B}_e| = \sqrt{B_1^2 + \left(\frac{\omega_0 - \omega}{\gamma}\right)^2} \tag{1.48}$$

On-resonance (i.e. when the frequency of the applied RF pulse $\omega$ equals the Larmor frequency $\omega_0$), Equation (1.48) reduces to $\mathbf{B}_e = \mathbf{B}_1$ and the magnetization simply rotates

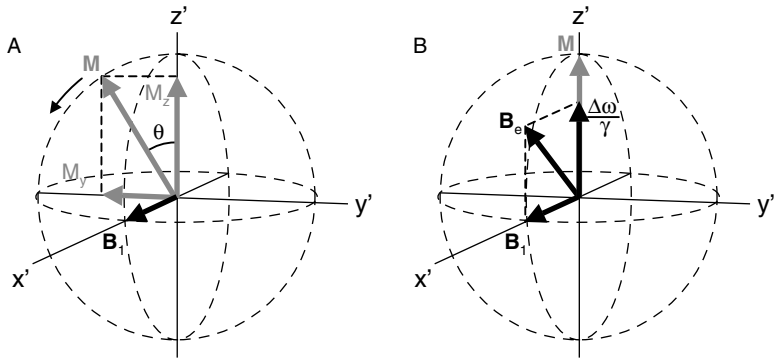


***Figure 1.6*** *Magnetic field vectors encountered in the rotating frame of reference x′y′z′ during excitation. (A) On-resonance, the effective, external magnetic field vector equals the magnetic field vector* $\boldsymbol{B}_1$ *along x′. The longitudinal magnetization experiences a torque and will rotate towards the transverse plane through an angle* θ. *(B) Off-resonance, the frequency of the magnetic field* $\boldsymbol{B}_1$ *no longer equals the Larmor frequency, resulting in an additional magnetic field vector* $\boldsymbol{\Delta\omega}/\gamma$ *along z′. The effective magnetic field* $\boldsymbol{B}_e$ *then equals the vector sum of* $\boldsymbol{B}_1$ *and* $\boldsymbol{\Delta\omega}/\gamma$. *The longitudinal magnetization will experience a torque from this effective field, resulting in a more complex rotation about* $\boldsymbol{B}_e$.

about $\mathbf{B}_1$ as shown in Figure 1.6A. In the event of a nonvanishing off-resonance vector (i.e. $\omega \neq \omega_0$), the effective magnetic field $\mathbf{B}_e$ is tilted from the transverse plane (Figure 1.6B). The magnetization will precess about $\mathbf{B}_e$, leading to a more complex rotation when compared with the on-resonance situation. Off-resonance effects during RF pulses (excitation) are discussed in detail in Chapter 5. For the remainder of this chapter it will be assumed that off-resonance effects are negligible.

## 1.7 Fourier Transform NMR

Following a RF pulse which is calibrated to rotate $\mathbf{M}_0$ by 90° (i.e. complete excitation), the magnetization is placed in the transverse plane of the rotating frame of reference. The magnetization precesses about $\mathbf{B}_0$ at the Larmor frequency and induces an emf in a receiving coil positioned in the transverse plane. Because of $T_2$ relaxation, the transverse magnetization and consequently the emf will decrease as a function of time. However, macroscopic and microscopic inhomogeneity in the main magnetic field $\mathbf{B}_0$ will create a distribution of locally different $\mathbf{B}_0$ magnetic fields across the sample, leading to a distribution of Larmor frequencies. When a macroscopic sample is considered, this distribution leads to a more rapid loss of transverse magnetization than caused by pure $T_2$ relaxation. The origin and compensation of $\mathbf{B}_0$ inhomogeneity is discussed in great detail in Chapter 10. For a sample with uniform proton density and $T_2$ relaxation constants, the acquired signal in the presence of magnetic field inhomogeneity can be described by:

$$M_{xy}(t) = M_{xy}(0)e^{-t/T_2}\int_r e^{+i\gamma\Delta B_0(r)t}dr = M_{xy}(0)e^{-t/T_2^*} \tag{1.49}$$

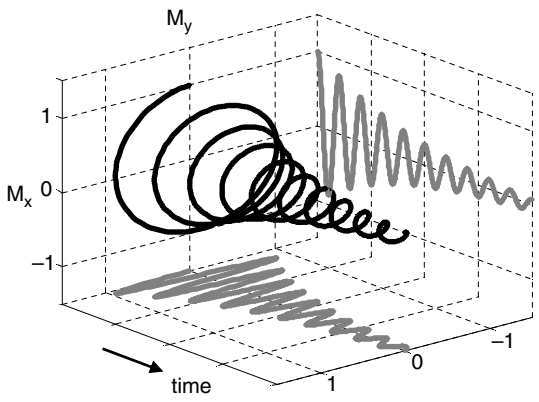


***Figure 1.7*** *The free induction decay (FID) of nuclear magnetization following an excitation pulse. The transverse magnetization precesses at the Larmor frequency and decays with a characteristic time constant $T_2^*$ as time progresses. The complex three-dimensional FID can be completely described by two projections on the ($M_x$, t) and ($M_y$, t) planes, corresponding to the real and imaginary components of the FID, respectively.*

where $\Delta B_0$ is indicative of $B_0$ inhomogeneity and equals $(B_0(\mathbf{r}) - B_{0,nom})$ where $B_0(\mathbf{r})$ is the magnetic field strength at position $\mathbf{r}$ and $B_{0,nom}$ represent the nominal magnetic field strength. $M_{xy}$ is the complex transverse magnetization ($M_{xy} = M_x + iM_y$). Note that even though the $T_2^*$ relaxation is often presented as a single-exponential decay, in practice it is a multi-exponential decay depending on the local $\mathbf{B}_0$ magnetic field inhomogeneity of individual spins as expressed by Equation (1.49).

The time-dependence of the emf (or signal intensity) is called the free induction decay (FID). The complex motion of the transverse magnetization as function of time can be represented as shown in Figure 1.7. NMR spectrometers separately detect the x and y components of this complex motion (see Chapter 10 for more details) and commonly the projections on the xt and yt planes are shown, which are given by:

$$M_x(t) = M_0 \cos[(\omega_0 - \omega)t + \phi]\, e^{-t/T_2^*} \tag{1.50}$$

$$M_y(t) = M_0 \sin[(\omega_0 - \omega)t + \phi]\, e^{-t/T_2^*} \tag{1.51}$$

where $\phi$ is the phase at $t = 0$. $M_x(t)$ and $M_y(t)$ are normally referred to as the real and imaginary FIDs, respectively. Although the FIDs hold all the relevant information about the nuclear spins, like their resonance frequencies and relative abundance, they are seldom used directly. Normally the time-domain data (i.e. the FID) is converted to frequency-domain data (i.e. the spectrum) by a Fourier transformation [17]. The Fourier transformation of a time-domain signal f(t) gives a frequency-domain signal $F(\omega)$ according to:

$$F(\omega) = \int_{-\infty}^{+\infty} f(t)e^{-i\omega t}dt \quad \text{or} \quad F(\nu) = \int_{-\infty}^{+\infty} f(t)e^{-i2\pi\nu t}dt \tag{1.52}$$

Fourier transformation is a reversible operation, so that a time-domain signal can be calculated from a frequency-domain signal with an inverse Fourier transformation given

by:

$$f(t) = \frac{1}{2\pi}\int_{-\infty}^{+\infty} F(\omega)e^{+i\omega t}d\omega \quad \text{or} \quad f(t) = \int_{-\infty}^{+\infty} F(\nu)e^{+i2\pi\nu t}d\nu \tag{1.53}$$

In principle it is possible to construct a spectrum from one of the components of the complex FID [i.e. either $M_x(t)$ or $M_y(t)$]. However, in that case negative and positive frequencies can not be discriminated since $\cos(\omega) = \cos(-\omega)$. Therefore, both components of the complex FID are measured, using so-called quadrature detection. More details about quadrature detection can be found in Chapter 10, while the characteristics of Fourier transformations are described in Appendix A3. Fourier transformation of the time-domain signals yields the real and imaginary frequency-domain signals (i.e. the spectrum) given by:

$$R(\omega) = A(\omega)\cos\,\phi - D(\omega)\sin\,\phi \tag{1.54}$$

$$I(\omega) = A(\omega)\sin\phi + D(\omega)\cos\phi \tag{1.55}$$

where

$$A(\omega) = \frac{M_0 T_2^*}{1 + (\omega_0 - \omega)^2 T_2^{*2}} \tag{1.56}$$

$$D(\omega) = \frac{M_0(\omega_0 - \omega)T_2^{*2}}{1 + (\omega_0 - \omega)^2 T_2^{*2}} \tag{1.57}$$

$A(\omega)$ and $D(\omega)$ describe the absorption and dispersion components of a Lorentzian lineshape and are drawn in Figure 1.8A. The width at half height, $\Delta\nu_{1/2}$, of the absorption component of a Lorentzian lineshape equals $1/(\pi T_2{}^*)$. The dispersive component is substantially broader, with a net integrated intensity of zero. Therefore, for the best separation (or resolution) of multiple lines in a NMR spectrum, absorption mode spectra are generally desired. However, when $\phi \neq 0$ a mixture of absorption and dispersion signals is observed (Figure 1.8B) as described by Equations (1.54) and (1.55) (Figure 1.8B). Pure absorption mode spectra can be obtained by 'phasing' the observed, mixed $R(\omega)$ and $I(\omega)$ spectra according to:

$$A(\omega) = R(\omega)\cos\,\phi_c + I(\omega)\sin\,\phi_c \tag{1.58}$$

$$D(\omega) = I(\omega)\cos\,\phi_c - R(\omega)\sin\,\phi_c \tag{1.59}$$

By interactively adjusting the phase $\phi_c$, absorption mode spectra are obtained when $\phi_c = \phi$ (Figure 1.8C). Due to hardware imperfections and/or timing errors the phase $\phi$ may depend upon the resonance frequency $\omega$. The simple 'zero-order' phase correction of Equations (1.58) and (1.59) is no longer adequate and one needs to resort to higher-order phase corrections as well. On most NMR spectrometers phase correction is performed according to:

$$\phi_c = \phi_0 + (\omega_0 - \omega)\phi_1 \tag{1.60}$$

where $\phi_0$ and $\phi_1$ are the zero and first order phase corrections, respectively. The adjustable phase $\phi_c$ therefore contains contributions from a constant phase correction $\phi_0$ for all resonances and a linear, frequency-dependent phase correction $\phi_1$. For some dedicated

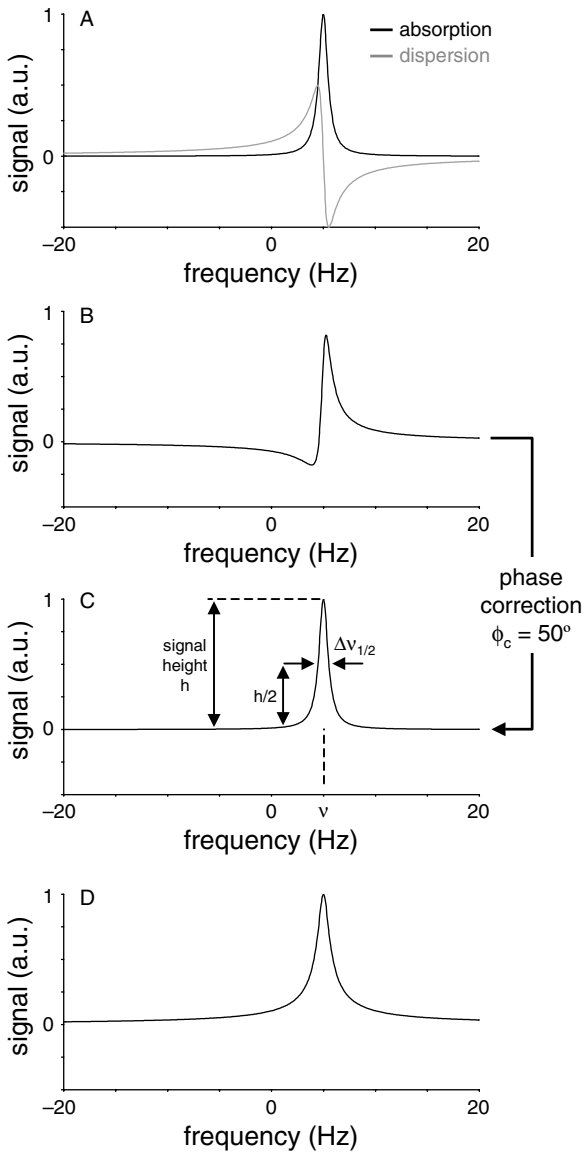


***Figure 1.8*** *Principle components of a NMR spectrum. (A) Complex Fourier transformation of an exponentially decaying FID gives rise to Lorentzian absorption and dispersion lineshapes. (B) In general, the initial phase of the FID is nonzero, such that a mixture of absorption and dispersion lineshapes is obtained. The dispersive component exhibits broad 'tails' which decreases the spectral resolution. The dispersive component can be eliminated by 'phasing' the spectrum, such that only the absorption component remains as shown in (C). From the phased spectrum, the frequency ν, the signal height h and linewidth at half height $\Delta\nu_{1/2}$ can be accurately measured. (D) Phase information is completely eliminated when presenting the spectrum in magnitude mode, given by the square root of the sums of the squares of the absorption and dispersion components [i.e. Equation (1.61)]. Because the dispersive component is included the resonance is substantially broader than the pure absorption lineshape.*

experiments even higher-order phase corrections may be necessary, but these will not be discussed here.

When the phase of the signal is not relevant, or if the phase can not be adjusted properly with zero- and first-order phase corrections (as in some two-dimensional NMR experiments, see Chapter 8), the signal can be presented in absolute value (or magnitude) mode. An absolute value signal is defined as:

$$M(\omega) = \sqrt{R(\omega)^2 + I(\omega)^2} \tag{1.61}$$

Figure 1.8D shows the absolute-value spectrum of the resonance line shown in Figure 1.8A. Because of the dispersive component, the resonance is much broader than in the corresponding phased spectrum (Figure 1.8C).

## 1.8 Chemical Shift

So far most of the descriptions assumed a macroscopic sample containing only one type of nuclear spin, having a resonance frequency given by Equation (1.11). If the frequency of nuclear spins were solely determined by the resonance condition of Equation (1.11), NMR spectroscopy would be of minor importance in chemistry and medicine. Nuclei of the same element (or isotope) even in different molecules, would resonate at the same frequency because of their identical gyromagnetic ratio. Fortunately, however, the resonance frequency $\omega$ not only depends on the gyromagnetic ratio $\gamma$ and the external magnetic field $B_0$, but is also highly sensitive to the chemical environment of the nucleus under investigation [5, 6]. This is commonly referred to as the chemical shift. The phenomenon of chemical shift is caused by shielding (screening) of nuclei from the external magnetic field by electrons surrounding them. Figure 1.9A shows a schematic representation of the electrons around a nucleus. When placed in an external magnetic field, the electrons will rotate about $\mathbf{B}_0$ in an opposite sense to the proton spin precession. Since this precession of electrons involves motion of charge, there will be an associated magnetic moment $\mu_e$, in analogy to the existence to a nuclear magnetic moment. The electron magnetic moment opposes the primary applied magnetic field $\mathbf{B}_0$. Therefore, the electrons will reduce the magnetic field that is sensed by the nucleus. This effect can be expressed in terms of an effective magnetic field $\mathbf{B}$ at the nucleus:

$$\mathbf{B} = \mathbf{B}_0(1 - \sigma) \tag{1.62}$$

where $\sigma$ is the shielding (or screening) constant. $\sigma$ is a dimensionless number [normally expressed in parts per million (ppm)], which depends on the chemical environment of the nucleus. Using Equation (1.62), the resonance condition of Equation (1.11) can be modified to:

$$\nu = \left(\frac{\gamma}{2\pi}\right) B_0(1 - \sigma) \tag{1.63}$$

Most often chemical shifts are not expressed in units of Hertz, since this would make chemical shifts dependent on the magnetic field strength. Instead chemical shifts are

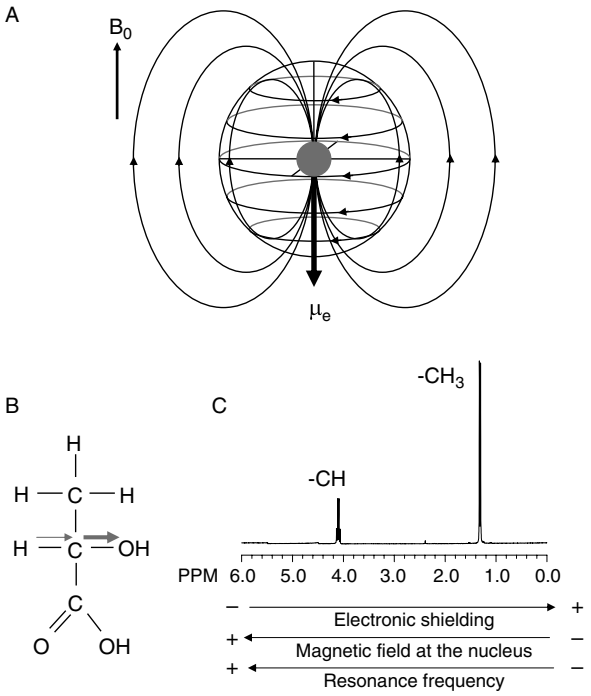


***Figure 1.9*** *Origin of the chemical shift. (A) The electrons surrounding a nucleus can be regarded as small currents, giving rise to a magnetic moment* $\boldsymbol{\mu}_e$ *at the nucleus. Since the magnetic moment opposes the external magnetic field, the effective magnetic field at the nucleus is reduced, thereby leading to a different Larmor frequency and hence a different chemical shift. The reduction of the effective magnetic field by surrounding electrons is often referred to as electronic shielding. (B) The electronegative oxygen atoms in lactate shift the electron density away from the protons, leading to reduced electronic shielding and thus to a higher Larmor frequency. (C) The proton NMR spectrum of lactate is readily explained by the fact that the methine proton is closer to electronegative oxygen atoms than the three methyl protons, thus leading to a higher Larmor frequency and chemical shift.*

expressed in terms of ppm. By convention the chemical shift δ is defined as:

$$\delta = \frac{\nu - \nu_{\text{ref}}}{\nu_{\text{ref}}} \times 10^6 \tag{1.64}$$

where $\nu$ and $\nu_{\text{ref}}$ are the frequencies of the compound under investigation and of a reference compound, respectively. The reference compound should ideally be chemically inert and its chemical shift should be independent of external variables (temperature, ionic strength, shift reagents) and should produce a strong (singlet) resonance signal well separated from all other resonances. A widely accepted reference compound for $^1$H and $^{13}$C NMR is tetramethylsilane (TMS) to which $\delta = 0$ has been assigned. However, the use of TMS is restricted to NMR on compounds in organic solvents. For aqueous solutions, 3-(trimethylsilyl) propionate (TSP) or 2,2-dimethyl-2-silapentane-5-sulfonate (DSS) are

typically used, of which DSS is more desirable as the chemical shift is temperature and pH independent [18]. Unfortunately, none of these compounds is found in *in vivo* systems and can therefore never be used as internal references. TSP and DSS can in principle be used as external reference compounds, being placed adjacent to the object under investigation. However, under these circumstances the observed chemical shift needs to be corrected for bulk magnetic susceptibility effects as well as macroscopic inhomogeneity of the main magnetic field (see Chapter 10). Differences in susceptibility and local magnetic field strength between the object under investigation and the adjacent external reference make the use of external chemical shift referencing undesirable. For *in vivo* applications other resonances have been used as an internal reference. Commonly used internal references are the methyl resonance of *N*-acetyl aspartate (2.01 ppm) for $^{1}$H MRS of the brain and the phosphocreatine resonance (0.00 ppm) for $^{31}$P MRS of brain and muscle.

## 1.9 Digital Fourier Transform NMR

The quality and/or information content of NMR spectra is determined by the signal-to-noise ratio (S/N) and the line width of the resonances. This relates through the Fourier transformation directly to the S/N and the $T_2{}^*$ relaxation decay of the FID. Next it will be demonstrated that the appearance of NMR spectra can be improved by specific manipulations of the FID.

### 1.9.1 Multi-scan Principle

The S/N can be improved by averaging, i.e. adding the FIDs of n consecutive, identical experiments leads to an improvement in S/N of a factor $\sqrt{\mathrm{n}}$ [19, 20]. This is because the voltage of the signal S increases linearly with n, while for the random processes of noise N the power increases linearly. Since power is proportional to the square of voltage, the noise voltage increases as $\sqrt{\mathrm{n}}$, leading to an overall improvement of the S/N of $\mathrm{n}/\sqrt{\mathrm{n}} = \sqrt{\mathrm{n}}$. In practice, the improvement in S/N of *in vivo* NMR by time-averaging is limited, since an improvement of a factor 10 requires a prolongation of measurement time by a factor $10^2 = 100$. Typically, an *in vivo* NMR experiment is a compromise between sufficient signal-to-noise and the allowable duration of the experiment.

### 1.9.2 Time-domain Filtering

Using Fourier transformation as the only data processing of the NMR time domain signals seldom results in an optimal frequency domain spectrum in terms of S/N, resolution or general appearance. Using the characteristics of the Fourier transformation (see Appendix A3), several manipulations prior to Fourier transformation can be performed on the NMR time domain signal to influence the S/N, resolution or remove broad background signals.

Apodization (or time-domain filtering) is a commonly used manipulation and essentially multiplies a time domain signal with a filter function, according to:

$$\mathrm{f_{filtered}}(\mathrm{t}) = \mathrm{f_{original}}(\mathrm{t}) \times \mathrm{f_{filter}}(\mathrm{t}) \tag{1.65}$$

where $\mathrm{f_{original}}(\mathrm{t})$ and $\mathrm{f_{filtered}}(\mathrm{t})$ are the original and filtered time-domain functions, respectively, and $\mathrm{f_{filter}}(\mathrm{t})$ is the applied filter function. Multiplication of two functions in the

time-domain is equivalent to the convolution of the Fourier transforms in the frequency domain, i.e.:

$$F_{filtered}(\omega) = FT[f_{filtered}(t)] = FT[f_{original}(t) \times f_{filter}(t)] = F_{original}(\omega) * F_{filter}(\omega) \quad (1.66)$$

where $*$ indicates the convolution between $F_{original}(\omega)$ and $F_{filter}(\omega)$. Some commonly used filter functions are:

1. Exponential weighting

$$f_{filter}(t) = e^{-t/T_w} \quad (1.67)$$

A decreasing monoexponential apodization function improves the S/N of the frequency-domain spectrum, since the (noisy) data points at the end of the FID are attenuated, while the data points at the beginning of the FID are relatively unaffected. Another consequence of the exponential weighting function is an increase in the resonance linewidths, since the apparent $T^*_{2w}$ becomes:

$$\frac{1}{T^*_{2w}} = \frac{1}{T^*_2} + \frac{1}{T_w} \quad (1.68)$$

If sufficient data have been recorded to minimize truncation artifacts ($t_{max} > 3T^*_2$), then optimal sensitivity is obtained by using a so-called matched filter in which $T_w = T^*_2$. The improved S/N comes at the expense of a doubling of the spectral linewidth, i.e. spectral resolution has been traded for sensitivity. Besides improving the S/N, this apodization can also be used on FIDs where the last data points have been truncated resulting in artifacts in the frequency domain (Figure 1.10F/G). For $T_w < 0$ the apodization leads to a resolution enhancement, since the apparent $T^*_{2w}$ becomes longer, resulting in line narrowing. However, the S/N is decreased since the data points at the end of the FID with relative high noise contribution are becoming more pronounced.

2. Lorentz–Gaussian transformation

$$f_{filter}(t) = e^{+t/T_L} e^{-t^2/T_G^2} \quad (1.69)$$

The Lorentz–Gaussian filtering function converts a Lorentzian lineshape to a Gaussian lineshape. A Gaussian lineshape decays to the baseline in a narrower frequency range as would a Lorentzian lineshape with the same linewidth at half height, i.e. a Lorentzian lineshape produces longer 'tails' which are a disadvantage when accurate determination (by integration) of overlapping resonance lines is required (Figure 1.11E). It is therefore sometimes advantageous to convert the theoretically predicted Lorentzian NMR lineshape to a more narrow Gaussian lineshape. The principle of the Lorentz–Gaussian transformation is to cancel (or decrease) the Lorentzian part of the FID [by multiplying with $\exp(+t/T_L)$, where $T_L = T^*_2$, such that $\exp(+t/T_L) \times \exp(-t/T^*_2) = 1$] while increasing the Gaussian character of the FID [by multiplying with $\exp(-t^2/T_G^2)$]. Using a sufficiently long $T_G$ value, a significant resolution enhancement can be achieved. Figure 1.11 shows the process of time-domain filtering on a $^{31}$P FID. Even though an increasing exponential filter (Figure 1.11C) and a Lorentz–Gaussian transformation can achieve the same resolution enhancement, the former is accompanied by a significant decrease in sensitivity, which can be minimal with a Lorentz–Gaussian transformation. In fact, the two adjustable parameters in Equation (1.69) can be used to improved the

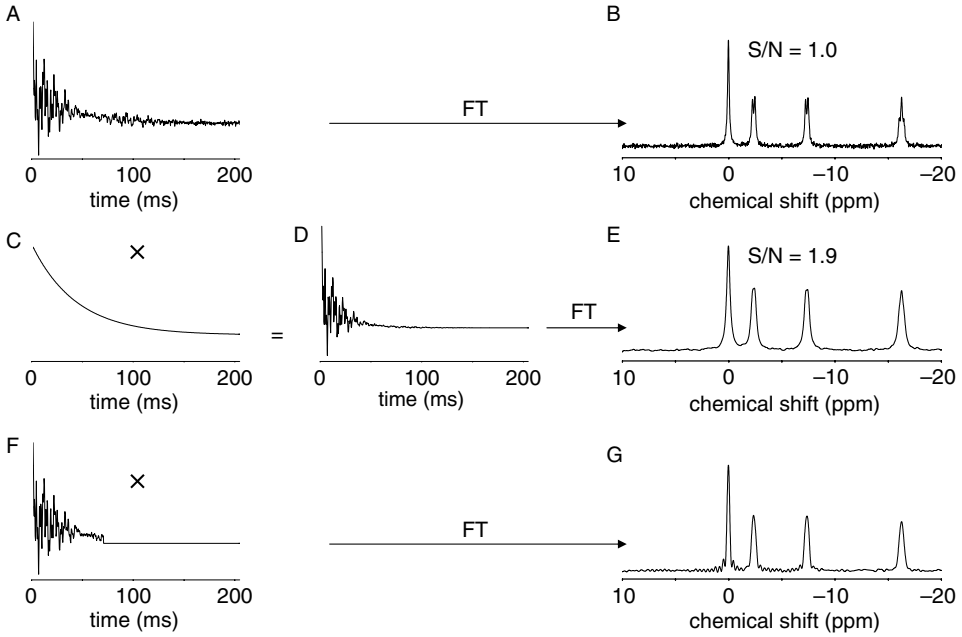


***Figure 1.10*** *The effects of time-domain apodization on the frequency-domain spectrum. (A) Fourier transformation of a $^{31}$P FID gives (B) a NMR spectrum composed of resonances from phosphocreatine and ATP. The spectral S/N, as defined as the peak height over the root mean square noise level, is typically not optimal. (C, D) Multiplication of the FID with a decaying exponential function will lead to (E) a significant increase in S/N, at the expense of a decrease in spectral resolution. (F) When time-domain acquisition has stopped before the NMR signal has decayed to zero, (G) the resulting NMR spectrum displays characteristic sinc-like wiggles. Apodization of the truncated time-domain signal can restore the Lorentzian lineshapes, giving a weighted FID and spectrum similar to those in (D) and (E).*

S/N without a significant decrease in spectral resolution (Figure 1.11F/G) or to improve the spectral resolution without a significant decrease in sensitivity (Figure 1.11H/I). Besides the mentioned, most commonly used apodization functions, a wide range of other functions are available each with specific characteristics regarding sensitivity and resolution [21].

### 1.9.3 Analog-To-Digital Conversion

So far the NMR signal has been described as a continuous, analog signal. However, the relatively simple but tedious Fourier transformation (and many other mathematical operations, like phasing and time domain filtering) are most conveniently performed by digital computer algorithms. As a consequence the analog FID signal received in the coil must be converted to a digital signal. This is done with an analog-to-digital converter (ADC), which measures the instantaneous value of the FID at equal time intervals (Figure 1.12). The speed of the analog-to-digital conversion is prescribed by the sampling theory [17]. This theory

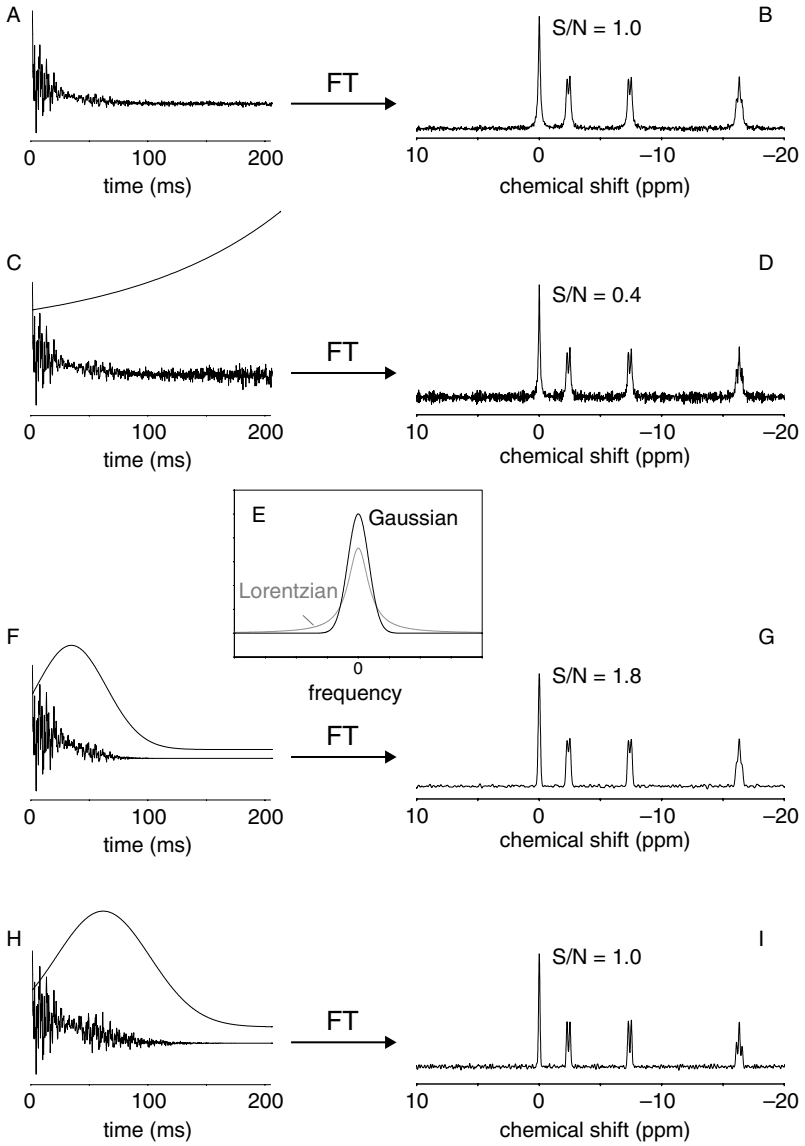


***Figure 1.11*** *The effects of time-domain apodization on the frequency-domain spectrum. (A, B) Time and frequency domain signals without apodization. The spectral S/N in (B) was assigned a relative value of 1.0. (C, D) Time-domain multiplication with an increasing exponential function improves the spectral resolution at the expense of a greatly reduced S/N. (E) Lorentzian and Gaussian resonance lines of equal FWHM and integrated amplitude. (F, G) Lorentz-to-Gauss transformation adjusted to give the same spectral resolution as in (B), results in an improved sensitivity. (H, I) When the Lorentz-to-Gauss transformation parameters are adjusted to provide the same spectral SNR as in (B), the spectral resolution is significantly improved.*

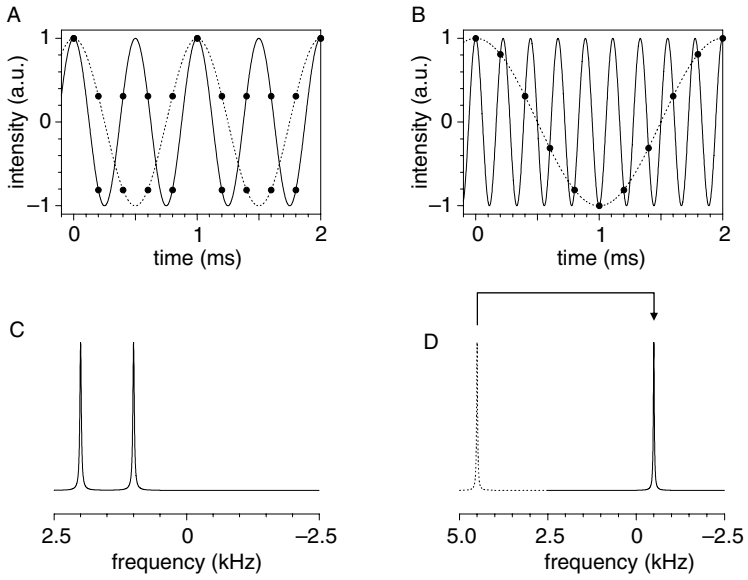


***Figure 1.12*** *Theory of analog-to-digital conversion. (A) A given time domain signal is sampled at 0.2 ms intervals, giving rise to a total spectral width of 5000 Hz and a Nyquist sampling frequency of 2500 Hz. The Larmor frequency of both resonances is smaller than the Nyquist sampling frequency, such that they can be adequately sampled. This gives a NMR spectrum (C) consisting of two resonances at the appropriate Larmor frequencies. (B) When the sample contains a resonance with a Larmor frequency* $\nu$ *above the Nyquist sampling frequency F, the signal is still sampled, but now at an apparent frequency* $\nu_0 - F + \nu$*, resulting in a NMR spectrum with a resonance at the incorrect, apparent frequency (D).*

states that any sinusoidal signal of frequency F can be accurately described when it is sampled at least twice per cycle. This minimum sampling rate is called the Nyquist frequency $F_{Nyquist}$. The spectral bandwidth SW equals $2F_{Nyquist}$, since frequencies between $-F_{Nyquist}$ and $+F_{Nyquist}$ are accurately sampled. The time between the data points is known as the dwell time and equals 1/SW. If a signal is present with an absolute frequency greater than the Nyquist frequency, then this signal will still be digitized, but at an incorrect frequency (Figure 1.12). A resonance with frequency $\nu_0 + F_{Nyquist} + \nu$, where $\nu_0$ is the center of the spectral bandwidth, will appear after Fourier transformation at a position with frequency $\nu_0 - F_{Nyquist} + \nu$. This so-called aliasing of resonances can be eliminated by increasing the spectral bandwidth, after which the minimum spectral bandwidth needed to unambiguously observe all the resonances can be determined. Aliasing of signal seems at first sight a large problem in FT NMR, since noise from outside the spectral region would be folded back into the spectrum thereby dramatically decreasing the obtainable S/N. However, high-frequency noise components can easily be filtered out before the ADC sampling by audio-filters (see Chapter 10). A cut-off filter, such as a Butterworth filter, does not affect signals within the spectral range, while suppressing (i.e. multiplying by zero) all signals (i.e. noise) outside the spectral range. To obtain optimal S/N without distortions from the cut-off points of

the filter, the filter bandwidth is normally set 10–25 % larger than the spectral width. More recent advances in digital electronics have led to the introduction of digital audio-filters with a much sharper cut-off profile.

### 1.9.4 Zero Filling

In general, the FID of a spectrum with spectral width $SW = 2F_{Nyquist}$ is sampled by the ADC over N points in accordance with the Nyquist sampling frequency. Through a discrete Fourier transformation, the NMR spectrum will also contain N points. The spectral resolution $\Delta\nu$ is therefore SW/N, which is equivalent to the reciprocal of the total acquisition (sampling) time $T_{acq}$, which is composed of N sampling periods of duration $\Delta t$:

$$\Delta\nu = \frac{1}{T_{acq}} = \frac{1}{N\Delta t} \tag{1.70}$$

For an experiment with 256 points sampled and $T_{acq} = 102.4$ ms, leading to $SW = 2F_{Nyquist} = 2500$ Hz, the spectral resolution is 9.77 Hz (2500 Hz/256). As can be seen from Figure 1.13, this spectral resolution is often too low to fully resolve the resonances present, i.e. it is desirable to have knowledge about the spectral amplitudes at intermediate frequencies. This can be achieved by decreasing the spectral width or by increasing the acquisition time. However, aliasing limits the increase in spectral resolution by decreasing the spectral width. Increasing the acquisition time will lead to increased data storage and an increase of the relative noise contribution as the signal intensity decreases with increasing acquisition time. Alternatively, the process of extending the acquisition time can be simulated by extending the acquired FID (which has decayed to zero amplitude) artificially by adding a string of points with zero amplitude to the FID prior to Fourier transformation. This process is known as zero filling. Figure 1.13 shows the effect of zero filling on the appearance of the β-ATP

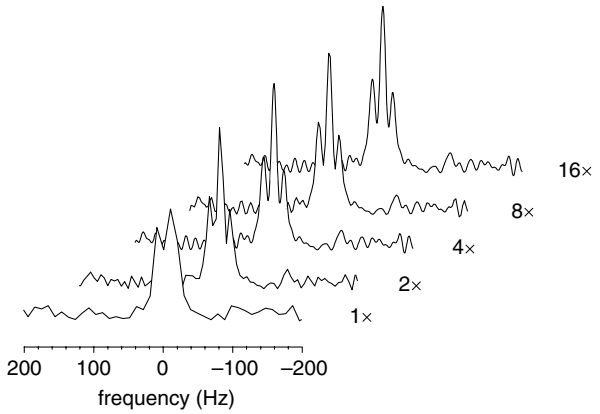


***Figure 1.13*** *Effect of zero filling on the spectral resolution. The triplet resonance of β-ATP is not well-resolved following a FT of the acquired data points (giving a spectral resolution of 9.77 Hz per point). Zero filling the original data (with a power of 2), completely resolves the triplet resonance (giving a spectral resolution of 0.61 Hz per point after 16 times zero filling). After four times zero filling no further improvement in spectral resolution is observed.*

resonance from a $^{31}$P spectrum. The relatively coarse spectral resolution results in an apparent doublet signal following direct Fourier transformation of the measured time domain signal. While the signal at intermediate frequencies is accurately digitized in the time-domain (since the frequencies are smaller than the Nyquist frequency), it is not visualized in the frequency-domain simply because the discrete Fourier transformation only calculates the signal at a limited number of discrete frequencies. Increasing the number of time domain points by zero filling allows the calculation of additional frequency domain points at intermediate frequencies, revealing the expected triplet structure for β-ATP. While zero filling does not increase the information content of the data, it can greatly improve the spectral appearance.

## 1.10 Spin–Spin Coupling

The NMR resonance frequencies, or chemical shifts, give direct information about the chemical environment of nuclei, thereby greatly aiding in the unambiguous detection and assignment of compounds. The integrated resonance area is, in principle (see Exercise 1.5 and Chapter 9), directly proportional to the concentration of the compounds, thereby making NMR a quantitative technique. An additional feature that can be observed in high-resolution NMR spectra is the splitting of resonances into several smaller lines, a phenomenon often referred to as scalar coupling, J coupling or spin-spin coupling [22]. Scalar coupling originates from the fact that nuclei with magnetic moments can influence each other, besides directly through space (dipolar coupling) also through electrons in chemical bonds (scalar coupling). Even though dipolar interactions are the main mechanism for relaxation in a liquid, there is no net interaction between nuclei since rapid molecular tumbling averages the dipolar interactions to zero. However, interactions through chemical bonds do not average to zero and give rise to the phenomenon of scalar coupling.

In the following a qualitative description of scalar coupling is given. A more quantitative description can be found in Chapter 8. Consider an isolated proton and an isolated carbon-13 atom as depicted in Figure 1.14A. Electrons in s-orbitals have a finite probability of being at the nucleus, giving rise to a hyperfine interaction between nuclear and electronic spins. The Fermi contact governs the interaction between the nuclear and electron spins and (energetically) *favors* an antiparallel over a parallel arrangement. In terms of energy level diagrams, the two separate (two-level) $^{1}$H and $^{13}$C energy level diagrams can be combined into one diagram (Figure 1.15A) with four energy levels, corresponding to the four nuclear spin combinations. The four allowed energy level transitions (for which the spin quantum number m changes by $\pm 1$) give rise to two resonance frequencies, $\nu_H$ at the proton frequency and $\nu_C$ at the carbon-13 frequency.

Now consider the situation where the proton and carbon-13 nuclei are covalently bound, as in [1-$^{13}$C]glucose (Figure 1.14B). The interaction between the two electrons inside a chemical bond is governed by the Pauli exclusion principle which *demands* that the electron spins are antiparallel. When both nuclear spins are antiparallel to the external magnetic field $B_0$, i.e. the high-energy ββ state, the two bonding electrons can not both be antiparallel to the nuclear spins, leading to an energetically less favorable state (Figure 1.15B). The ββ energy level increases by an amount proportional to $^{1}J_{HC}/4$ where $^{1}J_{HC}$ is the one-bond, heteronuclear scalar coupling constant. Similar arguments can be used

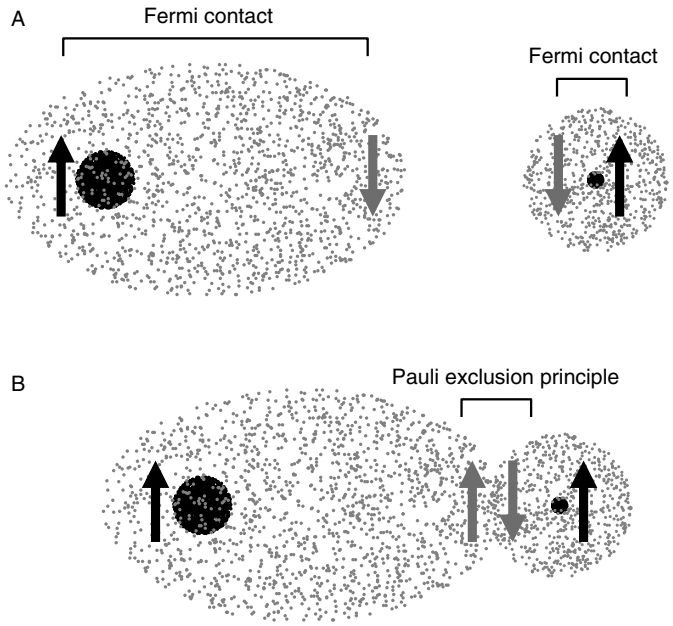


***Figure 1.14*** *Spin-spin interactions involved with scalar coupling. (A) In isolated atoms, the Fermi contact energetically favors an antiparallel orientation between nuclear and electronic spins. (B) In chemical bonds, the Pauli exclusion principle demands that the electron spins are in an antiparallel orientation thereby potentially forcing nuclear and electron spins in an energetically higher parallel orientation, depending on the nuclear spin state.*

to describe the energy increase for the $\alpha\alpha$ state. However, for the $\alpha\beta$ and $\beta\alpha$ states the electron spins can be antiparallel to the nuclear spins leading to an energetically more favorable situation. The energy level diagram for a scalar coupled two-spin system still only allows four transitions, but they now correspond to four different frequencies at $\nu_H + {}^1J_{CH}/2$ and $\nu_H - {}^1J_{CH}/2$ on the proton channel and at $\nu_C + {}^1J_{CH}/2$ and $\nu_C - {}^1J_{CH}/2$ on the carbon-13 channel. Each of the resonances has been divided into two new resonances of equal intensity separated by ${}^1J_{CH}$, giving rise to the NMR spectrum shown in Figure 1.16.

Similar arguments can be used to explain scalar coupling over two or three chemical bonds. While scalar coupling constants over one and three chemical bonds are typically positive, the scalar coupling constant over two chemical bonds is typically negative as can easily be deduced following arguments identical to those used for Figure 1.14. Because the basis of scalar coupling relies on magnetic interactions between electron spins and distant nuclear spins, the scalar coupling constant rapidly decreases with increasing number of chemical bonds and can typically be ignored for four or more bonds. The scalar coupling constant is independent of the applied external magnetic field, since it is based on the fundamental principle of spin-spin pairing and is therefore expressed in Hertz (Hz). Typical magnitudes of scalar coupling constants are: ${}^1H$-${}^1H$, 1–15 Hz; ${}^1H$-${}^{13}C$, 100–200 Hz; ${}^1H$-${}^{15}N$, 70–110 Hz; ${}^1H$-${}^{31}P$, 10–20 Hz; ${}^{13}C$-${}^{13}C$, 30–80 Hz; and ${}^{31}P$-O-${}^{31}P$, 15–20 Hz.

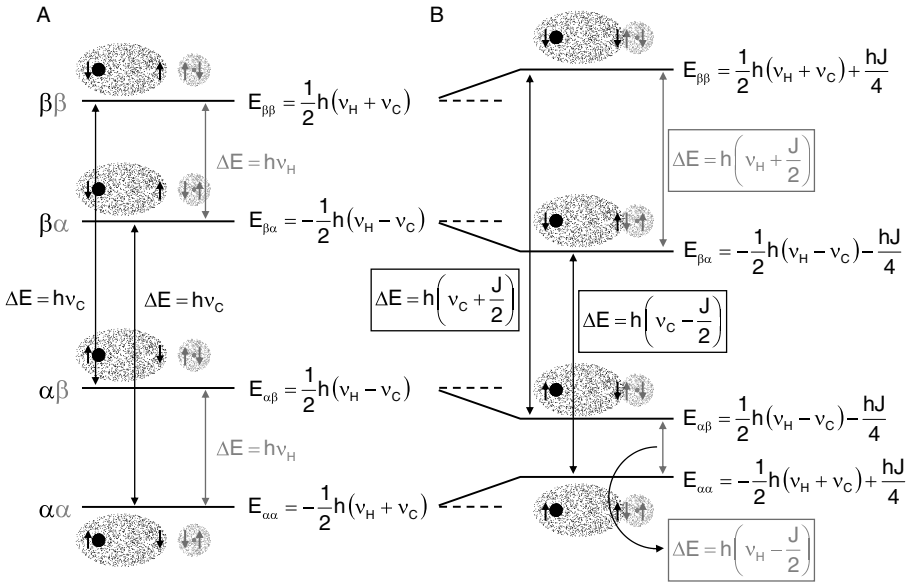


***Figure 1.15*** *Energy level diagram for (A) two isolated carbon-13 and proton nuclei and (B) a $^{13}$C-$^{1}$H 'molecule' with a covalent chemical bond between the carbon-13 and proton nuclei. The diagram in (A) is simply an extension of Figure 1.1B and allows two carbon-13 transitions with the same frequency $\nu_C$ and two proton transitions with the same frequency $\nu_H$ giving rise to singlet resonances in the carbon-13 and proton NMR spectra, respectively. When the carbon-13 and proton nuclei form a chemical bond, the nuclear spins affect each other through the bonding electrons. The $\beta\beta$ spin state (i.e. the nuclear spin for both $^{13}$C and $^{1}$H is in the $\beta$ state) becomes energetically less favorable as one of the two nuclear-electronic spin orientations is forced to be parallel. The same is true for the $\alpha\alpha$ spin state, whereas in the $\alpha\beta$ and $\beta\alpha$ spin states all spin orientations can be antiparallel. The same energy-level perturbations now give rise to two carbon-13 transitions with different frequencies, $\nu_C + J/2$ and $\nu_C - J/2$ and two protons transitions with different frequencies, $\nu_H + J/2$ and $\nu_H - J/2$, which will lead to the NMR spectra shown in Figure 1.16.*

All scalar coupling constants are for one chemical bond, except for $^{1}$H-$^{1}$H and $^{31}$P-O-$^{31}$P interactions which stretch over three and two bonds, respectively.

The situation shown in Figure 1.16 is only valid when the frequency difference between the two scalar-coupled spins is much larger than the scalar coupling between them. For a heteronuclear interaction as shown in Figure 1.15 this requirement is certainly valid, as the frequency difference is typically several tens of MHz, while the heteronuclear scalar coupling is less than 200 Hz. When the condition $|\nu_A - \nu_X| \gg J_{AX}$ holds, the two-spin AX spin system is referred to as a weakly coupled spin system and the corresponding NMR spectrum is often referred to as a first-order spectrum. However, for many homonuclear interactions the frequency difference $|\nu_A - \nu_B|$ is of the same order of magnitude as the homonuclear scalar coupling constant $J_{AB}$, giving rise to so-called strongly coupled spin systems. In a strongly coupled two-spin system, the $\alpha\beta$ and $\beta\alpha$ spin states become mixed, as summarized in Table 1.2. As a result of this mixing of spin states, the simple

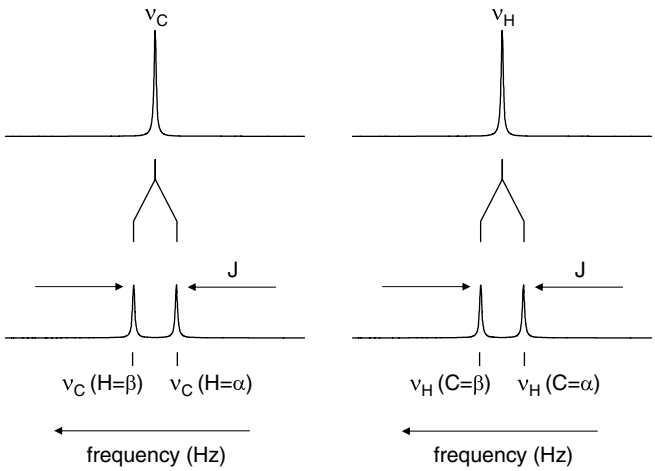


***Figure 1.16*** *Scalar coupling between carbon-13 and proton nuclei leads to a splitting of the singlet resonances into so-called doublet resonances. The resonances at the lower and higher frequencies are associated with energy level transitions in which the nuclear spin of the scalar-coupling partner is in the α and β spin-state, respectively.*

four-resonance-line spectrum (Figure 1.16) becomes more complicated as shown in Figure 1.17A and summarized in Table 1.3. The effects of strong coupling on the appearance of NMR spectra can not be understood in a classical sense, but requires full quantum-mechanical density matrix calculations [23]. Strongly coupled spin-systems produce so-called second-order spectra that are characterized by features not present in first-order spectra. Most noticeably from Figure 1.17A is the so-called 'roof effect' in which a line from the outer to the inner resonances forms an imaginary roof. This effect is another feature of NMR spectra that indicates that two multiplets belong to the same molecule and can therefore aid in the identification of compounds.

***Table 1.2*** *Energy characteristics for an AB spin system*

| Energy level | Spin function[a] | Energy[b] |
|---|---|---|
| 1 | $\beta\beta$ | $\frac{1}{2}h(\nu_A + \nu_B) + \frac{1}{4}hJ_{AB}$ |
| 2 | $\alpha\beta \cos\theta + \beta\alpha \sin\theta$ | $\frac{1}{2}hC - \frac{1}{4}hJ_{AB}$ |
| 3 | $\beta\alpha \cos\theta - \alpha\beta \sin\theta$ | $-\frac{1}{2}hC - \frac{1}{4}hJ_{AB}$ |
| 4 | $\alpha\alpha$ | $-\frac{1}{2}h(\nu_A + \nu_B) + \frac{1}{4}hJ_{AB}$ |

[a] $2\theta = \arcsin(J_{AB}/C)$.

[b] $C = \sqrt{(\nu_A - \nu_B)^2 + J_{AB}^2}$.

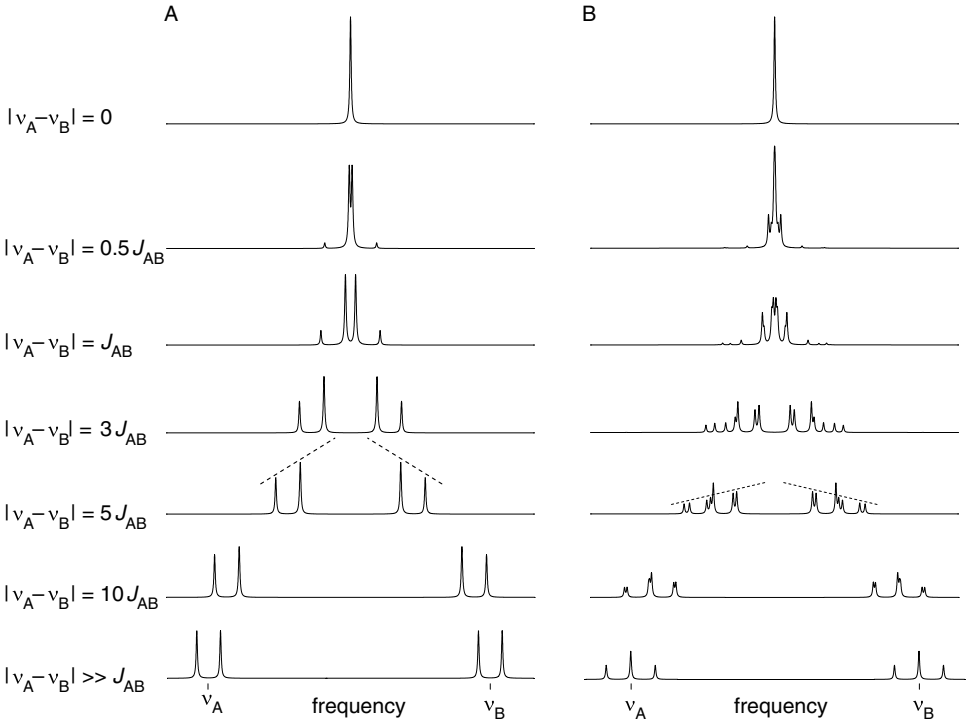


***Figure 1.17*** *Simulated (A) AB and (B) $A_2B_2$ NMR spectra showing the effects of varying the ratio of the scalar coupling constant to the frequency difference between the A and B resonances. The lower NMR spectra are indicative of weakly coupled AX and $A_2X_2$ spin systems, producing a first-order NMR spectrum, while the higher spectra are indicative of strongly coupled AB and $A_2B_2$ spin systems, displaying strong second-order effects, like the appearance of additional resonances, as well as the so-called 'roof effect' (dotted lines).*

### 1.10.1 Spectral Characteristics

To understand the splitting pattern encountered in NMR spectra of more complicated, but weakly coupled multi-spin systems, it is convenient to discriminate between nonequivalent, chemically equivalent and magnetically equivalent nuclei. For equivalent nuclei all physical and chemical properties (like reaction rates or exchange processes) are the same. The difference between chemically and magnetically equivalent nuclei is more subtle. Consider two nuclei with the same chemical shift, which are coupled to a third magnetic nucleus having a different chemical shift. When the scalar coupling constant of the two nuclei with the third nucleus is different, the nuclei are said to be chemically equivalent (since the chemical shift and therefore the chemical environment are identical) but not magnetically equivalent. For magnetically equivalent nuclei, the scalar coupling constant with a shared third nucleus must be identical.

***Table 1.3*** *Transition frequencies and relative intensities for an AB spin system*

| Transition | Frequency | Relative intensity |
|---|---|---|
| $1 \rightarrow 2$ | $\frac{1}{2}(\nu_A + \nu_B) + \frac{1}{2}J_{AB} - \frac{1}{2}C$ | $1 - \sin 2\theta$ |
| $1 \rightarrow 3$ | $\frac{1}{2}(\nu_A + \nu_B) + \frac{1}{2}J_{AB} + \frac{1}{2}C$ | $1 + \sin 2\theta$ |
| $3 \rightarrow 4$ | $\frac{1}{2}(\nu_A + \nu_B) - \frac{1}{2}J_{AB} - \frac{1}{2}C$ | $1 + \sin 2\theta$ |
| $2 \rightarrow 4$ | $\frac{1}{2}(\nu_A + \nu_B) - \frac{1}{2}J_{AB} + \frac{1}{2}C$ | $1 - \sin 2\theta$ |

Magnetically equivalent nuclei are always chemically equivalent and chemically equivalent nuclei can never produce a first-order spectrum. Keeping the issues of equivalence in mind, the appearance of first-order spectra can be predicted by some simple rules:

1. Magnetically equivalent nuclei do not produce an observable splitting of the corresponding resonance lines. This is because quantum mechanical selection rules prohibit the appropriate transitions. Therefore, for instance, there is no scalar coupling between the protons within an isolated methyl group ($CH_3$) even though they are only separated by two chemical bonds.
2. When there are more than two magnetic nuclei in a molecule, scalar coupling may occur between each pair of nuclei, resulting in a complex splitting pattern. The pattern for a given nucleus can be explained by the method of successive splitting. Consider three nonequivalent spins A, M and X (a so-called AMX spin system). The large difference in alphabetical order of the spins indicates a large difference in resonance frequency. An ABC spin system represents a scalar-coupled three-spin system with three nonequivalent spins which have similar chemical shifts (and do therefore not produce a first order spectrum). An $AX_2$ spin system represents a three-spin system with two nonequivalent nuclei (A and X) and two magnetically equivalent nuclei ($X_2$). The AMX spin system has spin-spin coupling between A and M (with $J_{AM}$) and between M and X (with $J_{MX}$). The splitting pattern of spin A is relatively simple, since it only experiences spin M. The resonance line of spin A will therefore be split in two lines separated by the scalar coupling constant $J_{AM}$. Similarly, the resonance for spin X is split once by the scalar coupling constant $J_{MX}$. However, the pattern for spin M is more complicated. First the coupling to spin A is considered resulting in two lines (a doublet), followed by the coupling to spin X, resulting in a splitting of each line in two more lines, giving a final 'doublet-of-doublets' (four lines of equal intensity).
3. The presence of magnetically equivalent nuclei in a group of interacting spins simplifies the appearance of the spectrum. The splitting pattern of spin A in an $AX_n$ spin system (where n is the number of magnetically equivalent spins) is simply given by a binomial distribution in which the lines are separated by the scalar coupling constant (e.g. $n = 2$ results in three lines with amplitudes in a 1:2:1 ratio).

Using these rules the appearance of all first-order spectra can be predicted. For example, Figure 1.18 shows the $^1H$ spectrum of lactic acid (lactate). Lactate can be seen as a $AX_3$ spin system, i.e. three magnetically equivalent methyl protons coupled to a single methine

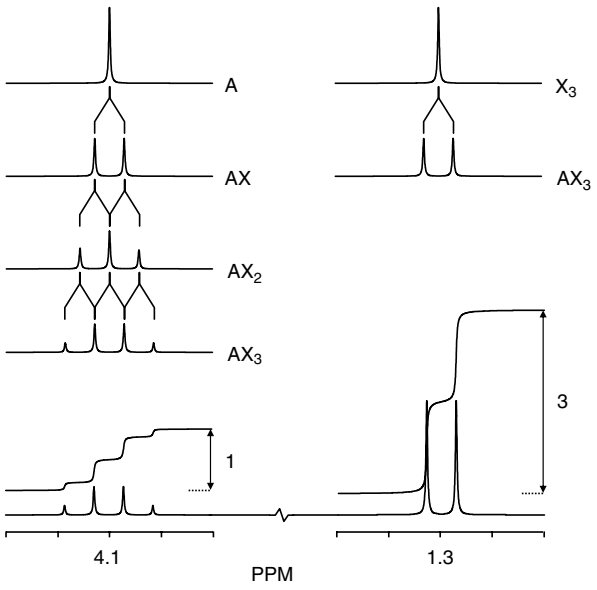


***Figure 1.18*** *The method of successive splitting for an $AX_3$ spin system (e.g. lactate, with a methyl group resonating at 1.31 ppm and a methine proton resonating at 4.10 ppm). The A resonance splits successively in a doublet, a triplet and a quartet, while the X resonance splits into a doublet. Note that the binomial distribution (e.g. 1:3:3:1 for a quartet) only arises for magnetically equivalent nuclei which have an identical scalar coupling constant with a common coupling partner. Since the multiplet resonances at 4.10 and 1.31 ppm originate from one and three protons, respectively, the relative integrated areas of the two multiplets are therefore also one and three.*

proton. Generally, the carbonyl and hydroxyl protons are invisible due to rapid exchange with water protons. Since the magnetically equivalent methyl protons do not produce any splitting among themselves, they only feel the methine proton, resulting in a doublet signal. The methine proton experiences three spins with an identical scalar coupling constant, resulting in four lines (a quartet) with a 1:3:3:1 binomial signal distribution. All the signals in the doublet and in the quartet are separated by the same scalar coupling constant. The relative *integrated* amplitude of the peaks at 1.31 ppm and 4.11 ppm is 3:1, respectively, since there are three methyl protons versus one methine proton.

In a two-spin system the effects of strong coupling changed the relative intensity and frequency of resonances (Figure 1.17A). However, in situations with more than two spins, like in a $A_2B_2$ four-spin system, the effects of strong coupling can also lead to additional resonances (Figure 1.17B). This is because the mixed energy levels allow energy transitions ($\Delta m = \pm 1$) that are simply not present when the energy levels are not mixed (i.e. when the spin-system is weakly coupled). It should be realized that while the behavior and spectral appearance of strongly coupled spin systems is no longer intuitive, it can still be quantitatively calculated through the use of the density matrix formalism, as will be discussed in Chapter 9. Note that the 'roof effect' is also visible for more complicated spin systems, as evident in Figure 1.17B.

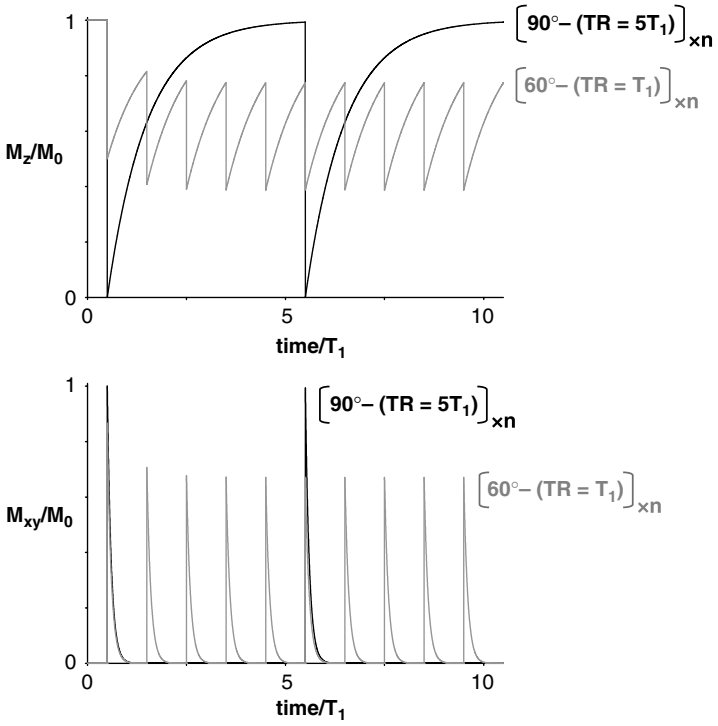


***Figure 1.19*** *The effects of multiple excitations and $T_1$ relaxation on the establishment of a longitudinal steady-state condition. When the repetition time TR is five times the $T_1$ relaxation time (black line) a steady-state situation is instantaneously achieved for which $M_{xy}(0) = M_0$. However, when TR < $5T_1$ (gray line), $T_1$ relaxation is incomplete in between excitations and a steady-state situation is achieved only following a number of excitations.*

## 1.11 $T_1$ Relaxation

In Section 1.6 $T_1$ and $T_2$ relaxation were introduced as the return of longitudinal magnetization following a perturbation and the disappearance of transverse magnetization, respectively. $T_1$ and $T_2$ relaxation are so fundamental to NMR that they essentially affect any NMR experiment. Knowledge of $T_1$ relaxation is required for signal quantification, the study of chemical exchange and the design of optimal timings for data acquisition. Consider a simple pulse-acquire experiment with an $\alpha^\circ$ excitation pulse and a repetition time TR. Figure 1.19 shows the amount of longitudinal magnetization over time when the sequence is continuously repeated, as would be the situation in the case of signal averaging. In the case of a 90° pulse the longitudinal magnetization is reduced to zero after each 90° pulse, after which it is allowed to recover through $T_1$ relaxation according to:

$$M_z(TR) = M_0(1 - e^{-TR/T_1}) \tag{1.71}$$

which reduces to $M_z(TR) = M_0$ for $TR > 5T_1$. The amplitude of the transverse magnetization is given by $M_{xy} = M_z \sin\alpha = M_0$. However, even though full excitation is achieved

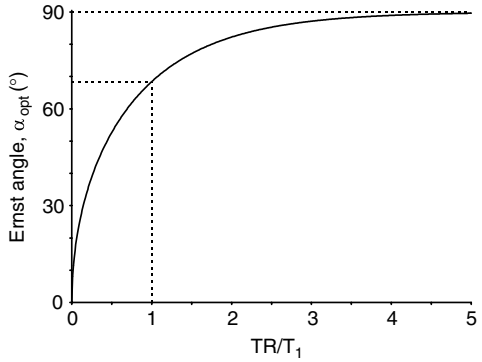


***Figure 1.20*** *Graphical representation of the relation between the optimal nutation angle (Ernst angle, in degrees) and the ratio of repetition time TR to the $T_1$ relaxation time of a ($\alpha^\circ$ - acquisition) experiment. The optimal nutation angle is the nutation angle which produces the highest S/N per unit of time for a given TR to $T_1$ ratio.*

during each scan, the experiment is not optimal in terms of signal per unit of time [$= 0.2(M_0/T_1)$] because the majority of scan time is used to wait for recovery of the longitudinal magnetization by $T_1$ relaxation. Repeating the experiment with a 60° excitation angle $TR = T_1$ results in the temporal $M_z$ and $M_{xy}$ modulations shown in Figure 1.19. During the first few scans the excitation pulse rotates more magnetization away from the longitudinal axis than can recover through $T_1$ relaxation. However, after about three scans the amount of signal decrease by excitation and signal recovery by $T_1$ relaxation are equal to each other, making the *steady-state* longitudinal magnetization prior to each excitation pulse equal to (see also Exercise 1.7):

$$M_z(\alpha, T_1) = \frac{M_0(1 - e^{-TR/T_1})}{(1 - \cos\alpha\, e^{-TR/T_1})} \tag{1.72}$$

Note that Equations (1.71) and (1.72) are both derived under the assumption that $M_{xy} = 0$ immediately prior to excitation. Experimentally this can be achieved by using $TR > 5T_2$ or by applying magnetic field gradient crushers to dephase any remaining transverse magnetization (see Chapter 4 for more details). For a 60° excitation pulse and $TR = T_1$ the signal per unit of time increases to $\sim 0.67(M_0/T_1)$. Even though the signal acquired per excitation is smaller as compared with $\alpha = 90^\circ$ and $TR = 5T_1$, the number of excitations per unit time has increased fivefold leading to a higher amount of acquired signal per unit time. It is straightforward to show (see also Exercise 1.7) that the optimal nutation angle $\alpha_{opt}$ for maximum signal per unit time is given by:

$$\alpha_{opt} = \arccos(e^{-TR/T_1}) \tag{1.73}$$

which is known as the Ernst angle. When $TR > 5T_1$, the exponential term vanishes and the optimal nutation angle is 90°. For shorter TR, the nutation angle gets smaller in order to reduce the saturation of longitudinal magnetization and to maximize the acquired signal. Figure 1.20 shows the Ernst angle as a function of $TR/T_1$. Note that in general signal acquisition should not begin until the steady-state condition underlying Equation (1.73)

has been reached. Experimentally this is achieved with so-called dummy scans which are identical to the real scan with the only difference that no data are acquired. The dummy scans help to achieve the steady-state condition, after which data acquisition can commence. Certain $\alpha$ and $TR/T_1$ combinations require several dozen dummy scans before the steady-state situation is achieved.

Data acquisition with a short repetition time and corresponding Ernst angle is frequently used in fast MRI (see Chapter 4), as well as in MRS on low-sensitivity nuclei, like phosphorus-31. But while the more efficient data acquisition improves the spectral S/N, it also introduces significant $T_1$ weighting which varies for metabolites with different $T_1$ relaxation times. Therefore, quantitative interpretation of metabolite spectra acquired under saturating conditions requires knowledge of the $T_1$ relaxation time.

The inversion recovery sequence is the classical 'gold-standard' for the determination of $T_1$ relaxation times. The inversion recovery method consists of two pulses and two delays. After full signal recovery during a long repetition time TR, the longitudinal magnetization is inverted by a 180° inversion pulse. The magnetization partially recovers during an inversion recovery delay t, after which the longitudinal magnetization is excited onto the transverse plane by a 90° excitation pulse. Following data acquisition, the sequence can be repeated, starting with recovery of longitudinal magnetization during the repetition time TR.

The signal intensity $M_z(t)$ during the recovery period t following the 180° inversion pulse can be described by:

$$M_z(t) = M_0 - (M_0 - M_z(0))e^{-t/T_1} \tag{1.74}$$

where $M_z(0)$ is the longitudinal magnetization at $t = 0$, immediately following the inversion pulse. For a perfect inversion pulse, $M_z(0) = -M_0$. The $T_1$ relaxation time constant can be obtained by acquiring NMR spectra (or images) at different recovery times t between 0 and $5T_1$. For $t = 0$, the inverted longitudinal magnetization has not yet recovered and is excited to the $-y'$ axis by a 90° pulse along the $-x'$ axis, resulting in a maximal negative resonance line after Fourier transformation. For $t = 5T_1$, the inverted magnetization has completely recovered to the $+z'$ axis and is excited to $+y'$, resulting in a maximal positive resonance line. Figure 1.21A shows typical inversion recovery spectra as a function of the recovery time t. Fitting the integrated resonance areas to Equation (1.74) gives an estimate of the $T_1$ relaxation time (Figure 1.21B). In general a three parameter fit [$M_0$, $M_z(0)$ and $T_1$] is preferred over a two-parameter fit (only $M_0$ and $T_1$), since the additional parameter makes the estimation of $T_1$ independent of the inversion accuracy or systematic offsets in the inversion recovery delays. A crude method of estimating the $T_1$ relaxation time constant is to determine the time of zero-crossing, $t_{null}$ in the recovery curve, after which the $T_1$ relaxation can be calculated as $T_1 = t_{null}/\ln 2$. Inversion recovery is a very reliable technique for the measurement of $T_1$, with an inherent insensitivity toward $B_0$ and $B_1$ magnetic field inhomogeneity. However, the technique is rather time-inefficient, since the experimental duration is dictated by the return of the thermal equilibrium magnetization following excitation. The low temporal resolution of inversion recovery has led to the development of many fast alternatives. Saturation recovery is a simple modification, in which the 180° inversion pulse is replaced by a 90° excitation pulse. Since the 90° excitation pulse reduces the longitudinal magnetization to zero at time $t = 0$, *irrespective* of the signal recovery prior to excitation, saturation recovery does not require a long repetition time, thereby significantly increasing the temporal resolution. Many other methods are more than an

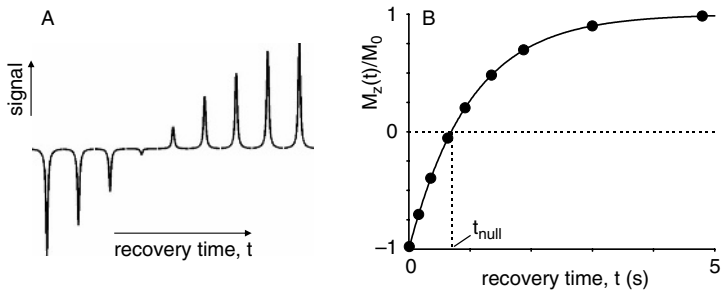


***Figure 1.21*** *Measurement of $T_1$ relaxation through the use of an inversion recovery method. (A) Upon inversion of the longitudinal magnetization, the magnetization relaxes back to its thermal equilibrium value with a $T_1$ relaxation time constant. Excitation at different inversion times results in spectra representing a discrete sampling of the $T_1$ recovery curve. (B) $T_1$ relaxation constants can be obtained by fitting the spectra in (A) with Equation (1.74). The time of zero-crossing ('nulling') of the longitudinal magnetization, $t_{null,}$ is given by $T_1 ln2$ and can provide a crude estimate of $T_1$.*

order of magnitude faster than inversion recovery and some will be discussed in terms of fast $T_1$ mapping by MRI (Chapter 4). However, it should be realized that the increased time resolution is often traded for increased sensitivity towards experimental imperfections, like $B_1$ magnetic field inhomogeneity, decreased S/N or sufficient accuracy over only a limited range of $T_1$ relaxation times.

## 1.12 $T_2$ Relaxation and Spin-echoes

The observation of NMR signal depends upon the generation of phase coherence. The existence of phase coherence is finite due to $T_2^*$ relaxation. According to Equation (1.49), $T_2^*$ relaxation is composed of intrinsic $T_2$ relaxation and dephasing by macroscopic and microscopic magnetic field inhomogeneity. Following a 90° pulse, phase coherence is generated which disappears with a time constant $T_2^*$, thereby obscuring any information about $T_2$. However, through the generation of so-called spin-echoes [24] it is possible to separate the contribution of $T_2$ and magnetic field inhomogeneity. The simplest experiment to generate spin echoes (and obtain information on $T_2$) is the Hahn sequence [24] of two RF pulses shown in Figure 1.22A. An initial 90° RF pulse (irradiated along the −x axis of the rotating frame, i.e. $90°_{-x}$) creates transverse magnetization (phase coherence) along the y axis (Figure 1.22B). During the subsequent delay the magnetization starts losing coherence, since spins experience, besides the intrinsic $T_2$ relaxation, a range of $B_0$ magnetic fields and therefore precess about z with a variety of Larmor frequencies (Figure 1.22C). In other words, spins at different spatial positions acquire different phases due to variations in the main magnetic field. The phase $\phi(\mathbf{r})$ acquired by spins at position $\mathbf{r}$ is given by $\phi(\mathbf{r}) = \gamma \Delta B_0(\mathbf{r})TE/2$, where $\Delta B_0(\mathbf{r})$ represents the magnetic field inhomogeneity, being the difference between the magnetic field at position $\mathbf{r}$, $B_0(\mathbf{r})$ and the nominal magnetic field across the entire sample, $B_{nom}$. After the delay TE/2, a $180°_y$ RF pulse is applied to the sample, which causes all magnetization vectors to rotate about y by 180°, leading to a

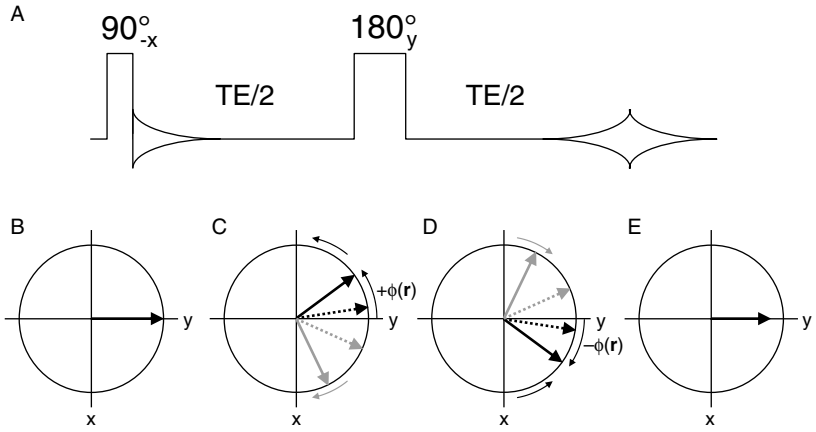


***Figure 1.22*** *Spin-echo formation for uncoupled spins. In a spin-echo experiment (A), the spins are excited (B) after which they dephase in the transverse plane during the first half of the echo time, due to $B_0$ magnetic field inhomogeneity and frequency offsets (C). A 180° refocusing pulse mirrors all magnetization vectors along the y axis (D) after which the spins rephase during the second half of the echo time due to the same $B_0$ magnetic field inhomogeneity and frequency offsets. At the echo time TE, the rephasing is complete and a spin-echo is formed (E). Obviously, the signal has decayed due to $T_2$ relaxation.*

resetting of the acquired phase from $+\phi(\mathbf{r})$ to $-\phi(\mathbf{r})$. During a second delay TE/2 the spins precess again at their local Larmor frequencies (Figure 1.22D) and because the phase was reset by the 180° pulse, the spins will be refocused along the y' axis at the end of the second delay to form a spin echo (Figure 1.22E). The time between the 90° pulse and the top of the spin-echo (i.e. where optimal refocusing occurs) is referred to as the echo time TE. At the top of the echo, the effects of $B_0$ magnetic field inhomogeneity are refocused (i.e. their phase effect is eliminated) and the signal decrease is caused exclusively by inherent $T_2$ relaxation (neglecting diffusion effects). The spin echo experiment is one of the most important elementary pulse sequences for *in vivo* NMR spectroscopy. Spin-echoes form the basis for spatial localization, water suppression, spectral editing and a wide range of additional delayed-acquisition methods. Spin echo techniques can also be used to filter out components with short $T_2$ relaxation times and they allow the acquisition of an artifact-free FID (e.g. the second half of the echo). This is because in a simple 90° pulse-acquire experiment, the first points of the FID can be distorted due to the close proximity of a high power 90° pulse (i.e. breakthrough of RF power). Furthermore, the spin-echo sequence can be used to measure the $T_2$ relaxation time by performing several experiments in which the echo time is varied (Figure 1.23). The corresponding spectra can be fitted to an exponential curve, according to:

$$M_{xy}(TE) = M_{xy}(0)e^{-TE/T_2} \tag{1.75}$$

to obtain the $T_2$ relaxation time constant. An alternative method to measure $T_2$ is the Carr–Purcell–Meiboom–Gill (CPMG) experiment [25, 26], in which the single 180° refocusing pulse is replaced by a train of successive 180° pulses. The main advantage of the

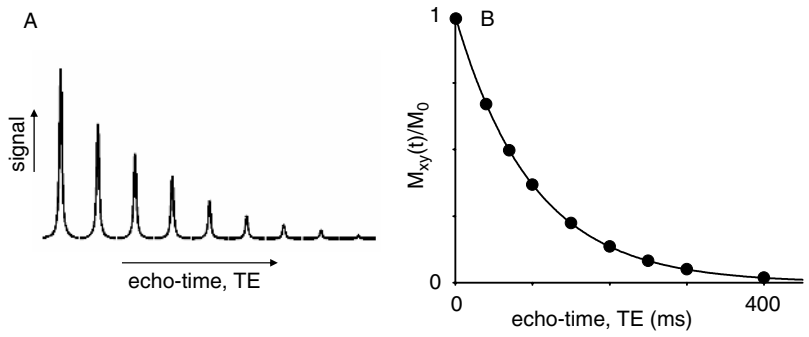


***Figure 1.23*** *Measurement of $T_2$ relaxation through the use of a spin-echo method. (A) NMR spectra obtained at different echo times. (B) the $T_2$ relaxation time constants can be obtained by fitting the data presented in (A) with Equation (1.75).*

CPMG method is that signal loss during the echo time as a result of diffusion is greatly reduced, such that the measured $T_2$ relaxation time constant is closer to the intrinsic, dipolar $T_2$ relaxation time constant. The effects of diffusion are detailed in Chapter 3.

## 1.13 Exercises

**1.1** A 2 L water-filled sphere (T = 298.15 K) is placed inside a 3.0 T MR magnet.

**A** Calculate the net access of proton spins in the low-energy α-state (hint: water density = 1.00 g $mL^{-1}$ and Avogadro constant = $6.02214 \times 10^{23}$ $mol^{-1}$).

**B** Calculate the error that is made by ignoring all higher order terms in the Taylor expansion of Equation (1.23) for T = 298.15 K, 4.0 K and 0.01 K.

**1.2** Derive the Bloch equations in the laboratory frame in the absence of relaxation [Equations (1.33)–(1.35)] from Equation (1.28).

**1.3** Show that free precession of the transverse magnetization according to:

$$M_x(t) = M_x(0)\cos \omega t + M_y(0)\sin\ \omega t$$

and

$$M_y(t) = M_y(0)\cos \omega t - M_x(0)\sin\ \omega t$$

is a solution of the Bloch equations in the laboratory frame [Equations (1.33)–(1.35)] in the absence of a perturbing magnetic RF field.

**1.4** **A** Derive the Bloch equations in the rotating frame [Equations (1.45)–(1.47)] from the Bloch equations in the laboratory frame [Equations (1.39)–(1.41)].

**B** Show that Equations (1.50) and (1.51) are solutions of the Bloch equations in the rotating frame (assume that $T_2 = T_2^*$).

**1.5** **A** Derive the expression for the full line width at half maximum (FWHM) for the absorption component of a Lorentzian line [e.g. Equation (1.56)].

**B** Derive the expression for the FWHM for the magnitude component of a Lorentzian line.

**C** Derive the expression for the absorption and dispersion parts of a resonance line originating from a full spin-echo (as opposed to a FID).

**D** Determine the peak heights and integrals of (the absorption component of) Lorentzian lines originating from a FID and a full spin-echo.

**1.6** Longitudinal magnetization can be 'excited' into the transverse plane by a 90° (or $\pi/2$) pulse.

**A** Starting from the Bloch equations in the rotating frame, derive an expression for the conversion of longitudinal magnetization $M_z$ into transverse magnetization $M_y$ by a RF pulse of length T and amplitude $B_1$ applied on-resonance along the $x'$ axis. Ignore $T_1$ and $T_2$ relaxation. Show how the nutation angle depends on the pulse amplitude and length.

**B** If the pulse length of the 90° pulse is 1.0 ms, what is the required $B_1$ magnitude in $\mu$T to achieve excitation?

**C** How many Larmor precession cycles will occur in the laboratory frame at $B_0 =$ 3.0 T during the 90° excitation pulse?

**1.7** Consider a pulse-acquire experiment consisting of a RF pulse generating a nutation angle $\alpha$ followed by a recovery time TR.

**A** Starting with the Bloch equation for $T_1$ relaxation [i.e. Equation (1.38)] derive an expression for the recovery of the longitudinal magnetization following a perturbation.

**B** Derive the expression for the steady-state longitudinal magnetization [i.e. Equation (1.72)] for the pulse-acquire sequence.

**C** Calculate after how many experiments the longitudinal magnetization is within 1 % of the steady-state magnetization when $\alpha = 40°$ and $TR = T_1$.

**D** Suppose that 10 blocks of four averages are acquired sequentially in one experiment with $\alpha = 40°$ and $TR = T_1$ starting from an initial thermal equilibrium situation. Calculate the difference between the acquired signal in the first and the last block due to incomplete $T_1$ saturation during the first block.

**E** Derive the Ernst angle expression from Equation (1.72).

**F** Calculate the Ernst angle for the excitation pulse of a spin-echo sequence with $TR = 0.5T_1$. Assume negligible $T_1$ relaxation during the echo time TE.

**1.8** In a properly executed spin-echo sequence, the resonances of all (uncoupled) spins appear with the same relative phase. The absolute phase of all resonances can be made zero by a simple zero-order phase correction.

**A** Calculate the phase difference between the creatine methyl (3.03 ppm) and NAA methyl (2.01 ppm) proton resonances at 7.05 T in the presence of a 500 $\mu$s timing error.

**B** In a proton spectrum acquired at 4.0 T (water is on-resonance at 4.7 ppm), the choline methyl (3.22 ppm) and NAA methyl (2.01 ppm) resonances appear with relative phases of 30° and 210°, respectively. Calculate the required zero- and first-order phase corrections to properly phase the spectrum to pure absorption lines.

**1.9** Given the Gaussian line shape:

$$F_G(\omega) = \sqrt{\frac{\pi}{4}} M_0 T_{2G} e^{-\frac{(\omega_0-\omega)^2 T_{2G}^2}{4}}$$

**A** Find the expression for the FWHM.
**B** For single Lorentzian and Gaussian resonance lines of equal line width and area, calculate the signal height-to-noise advantage of a Gaussian line (assuming equal noise levels).
**C** For single Lorentzian and Gaussian resonance lines of equal line width and area, calculate the line width advantage of a Gaussian line at 10 % of the respective peak heights.

**1.10** Consider a (hypothetical) $^1$H NMR spectrum with the following five resonances:

Resonance 1: triplet resonance ($^3J_{HH} = 7$ Hz) at 1.1 ppm with relative intensity (as determined by numerical integration) of 307.
Resonance 2: quartet resonance ($^3J_{HH} = 7$ Hz) at 3.9 ppm with relative intensity 198.
Resonance 3: doublet-of-doublets ($^3J_{HH} = 11$ and 8 Hz) at 7.2 ppm with relative intensity 102.
Resonance 4: doublet resonance ($^3J_{HH} = 8$ Hz) at 8.5 ppm with relative intensity 105.
Resonance 5: doublet resonance ($^3J_{HH} = 11$ Hz) at 10.0 ppm with relative intensity 96.

With the knowledge that the $^1$H NMR spectrum originates from an organic molecule $C_5H_8O_2$, determine the complete chemical structure of the compound.

**1.11** Consider a weakly coupled four-spin system $AMX_2$ with chemical shift positions given by $\delta_A = 5.0$ ppm, $\delta_M = 1.5$ ppm and $\delta_X = 3.0$ ppm relative to a carrier frequency of 200 MHz.

**A** Sketch the NMR spectrum for this compound when $J_{AM} = 20$ Hz, $J_{MX} = 10$ Hz and $J_{AX} = 0$ Hz. Assume equal $T_1$ and $T_2$ characteristics for all resonances.
**B** Sketch the NMR spectrum for this compound when $J_{AM} = 20$ Hz, $J_{MX} = 10$ Hz and $J_{AX} = 5$ Hz. Assume equal $T_1$ and $T_2$ characteristics for all resonances.
**C** When the NMR spectrum is acquired with a pulse-acquire sequence ($\alpha = 90^\circ$, TR = 0.5 s, number of averages 8 192) sketch the NMR spectrum for this compound when $J_{AM} = 0$ Hz, $J_{MX} = 10$ Hz and $J_{AX} = 0$ Hz and $T_{1A} = 5.0$ s, $T_{1M} = 1.0$ s, $T_{1X} = 2.0$ s. Assume equal $T_2$ characteristics for all resonances.

**1.12** A proton NMR signal is acquired as 512 complex points during an acquisition time of 102.4 ms.

**A** Determine the spectral width of the experiment.
**B** Determine the apparent spectral frequency position of a signal with a frequency of +3800 Hz.
**C** Determine the apparent spectral frequency position of a signal with a frequency of −16 000 Hz.

**1.13** In a proton NMR spectrum the resonance from 2,2-dimethyl-2-silapentane-5-sulfonate (DSS) is detected at 170.345213 MHz. Two other resonances occur at 170.345453 MHz and 170.345668 MHz, respectively.

**A** Calculate the chemical shifts of the two resonances in PPM.
**B** Calculate the frequencies of the two compounds at 7.05 T when DSS appears at a frequency of 300.176544 MHz.

**1.14** The time domain data from a sample consists of three sinusoidal functions ($M_0$ = 150, 300 and 200) oscillating at different frequencies (250, 300 and 500 Hz) and decaying at different rates ($T_2$ = 50, 50 and 100 ms).

**A** Sketch the Fourier transform spectrum acquired from the sample when the initial phase is zero for all resonances. Indicate linewidths (in Hz) and relative peaks heights.

**B** Sketch the Fourier transform spectrum acquired from the sample when the initial phases are 0°, 90° and 135°, respectively.

**1.15** Show that the real and imaginary frequency domain signals given by Equations (1.54) and (1.55) reduce to pure absorption and dispersion signals following a phase correction according to Equations (1.58) and (1.59) with $\phi_c = \phi$.

**1.16** Hund's rule states that if two or more empty orbitals are available, electrons occupy each with spins parallel until all orbitals have one electron. When chemical bonds in $sp^3$ hybridized structures are considered, describe the signs of $^2J_{HH}$ and $^3J_{HH}$ relative to $^1J_{CH}$ using similar arguments as used for Figures 1.14 and 1.15.

## References


1. Purcell EM, Torrey HC, Pound RV. Resonance absorption by nuclear magnetic moments in a solid. *Phys Rev* **69**, 37–38 (1946).
2. Bloch F, Hansen WW, Packard ME. Nuclear induction. *Phys Rev* **69**, 127 (1946).
3. Bloch F. Nuclear induction. *Phys Rev* **70**, 460–473 (1946).
4. Bloch F, Hansen WW, Packard ME. The nuclear induction experiment. *Phys Rev* **70**, 474–485 (1946).
5. Proctor WG, Yu FC. The dependence of a nuclear magnetic resonance frequency upon chemical compound. *Phys Rev* **77**, 717 (1950).
6. Dickinson WC. Dependence of the F19 nuclear resonance position on chemical compound. *Phys Rev* **77**, 736 (1950).
7. Ernst RR, Anderson WA. Applications of Fourier transform spectroscopy to magnetic resonance. *Rev Sci Instrum* **37**, 93–102 (1966).
8. Shaw TM, Elsken RH. Nuclear magnetic resonance absorption in hygroscopic materials. *J Chem Phys* **18**, 1113–1114 (1950).
9. Odebald E, Lindstrom G. Some preliminary observations on the proton magnetic resonance in biological samples. *Acta Radiol* **43**, 469–476 (1955).
10. Damadian R. Tumor detection by nuclear magnetic resonance. *Science* **171**, 1151–1153 (1971).
11. Moon RB, Richards JH. Determination of intracellular pH by $^{31}P$ magnetic resonance. *J Biol Chem* **248**, 7276–7278 (1973).
12. Hoult DI, Busby SJ, Gadian DG, Radda GK, Richards RE, Seeley PJ. Observation of tissue metabolites using $^{31}P$ nuclear magnetic resonance. *Nature* **252**, 285–287 (1974).
13. Lauterbur PC. Image formation by induced local interactions: examples employing nuclear magnetic resonance. *Nature* **242**, 190–191 (1973).
14. Mansfield P, Grannell PK. NMR 'diffraction' in solids? *J Phys C: Solid State Phys* **6**, L422–L427 (1973).
15. Munowitz M. *Coherence and NMR*. John Wiley & Sons, Ltd, Chichester, 1988.
16. Bloch F, Siegert A. Magnetic resonance for nonrotating fields. *Phys Rev* **57**, 522–527 (1940).
17. Bracewell RM. *The Fourier Transform and its Applications*. McGraw-Hill, New York, 1965.
18. Wishart DS, Bigam CG, Yao J, Abildgaard F, Dyson HJ, Oldfield E, Markley JL, Sykes BD. $^1H$, $^{13}C$ and $^{15}N$ chemical shift referencing in biomolecular NMR. *J Biol NMR* **6**, 135–140 (1995).

19. Ernst RR. Sensitivity enhancement in magnetic resonance. *Advances in Magnetic Resonance*. Volume **2**. Academic Press, New York, 1966.
20. Traficante DD. Time averaging, does the noise really average towards zero? *Concepts Magn Reson* **3**, 83–87 (1991).
21. Ernst RR, Bodenhausen G, Wokaun A. *Principles of Nuclear Magnetic Resonance in One and Two Dimensions*. Clarendon Press, Oxford, 1987.
22. Ramsey NF, Purcell EM. Interactions between nuclear spins in molecules. *Phys Rev* **85**, 143–144 (1952).
23. Goldman M. *Quantum Description of High-Resolution NMR in Liquids*. Oxford University Press, Oxford, 1991.
24. Hahn EL. Spin echoes. *Phys Rev* **80**, 580–594 (1950).
25. Carr HY, Purcell EM. Effects of diffusion on free precession in nuclear magnetic resonance experiments. *Phys Rev* **94**, 630–638 (1954).
26. Meiboom S, Gill D. Modified spin-echo method for measuring nuclear relaxation times. *Rev Sci Instrum* **29**, 688–691 (1958).